Basic ingredients, development of phenomenological models and practical use of crystal plasticity

Georges Cailletaud
MINES ParisTech
Centre des Matériaux, CNRS UMR 7633

Abstract This part is an introduction to phenomenological crystal plasticity models, to their properties and their use either in component calculations or in microstructure modelling. Time dependent or time independent versions of the models are presented. The applications deal with single crystal or polycrystalline materials. In this last case, the aggregate is modelled either by a finite element mesh, in order to represent the local microstructure, or by using so called uniform fields models, which allow to introduce the average effect of each crystalline phase in the global behaviour.

1 Introduction

The theoretical framework needed to develop single crystal models has been built in the seventies (Mandel, 1971; Hill, 1966; Hill and Rice, 1972; Rice, 1970, 1971; Asaro and Rice, 1977), and the first practical applications a few years later (Asaro, 1983a,b). The history of crystal plasticity is then well known, and can be reviewed in classical books (Havner, 1992; Teodosiu, 1997). The purpose of this section is then not to add a new description of rather classical approaches, but to enter the topic according to an alternative route, namely the framework of thermodynamics of irreversible processes, and to present a mechanical approach, seen as a multipotential theory, and to illustrate its capabilities by a series of examples.

The interest of this thermodynamical approach is to provide natural schemes for the choice of the evolution equations and the type of the hardening variables. The deformation mechanisms are restricted to slip, on given planes and along given directions. This class of model can be applied to single crystal or polycrystal description. Single crystal slip is illustrated in Fig.1, which shows the development of plasticity on a Ni-base superalloy specimen, after 1, 2 and 11 cycles: a first plane is activated after the initial

tension; more and more slip activity can be observed after 2 and 11 cycles. The crystal was oriented for single slip, so that only one line can be seen. Multiple slip can also be found, depending on the orientation of the specimen. In polycrystals, various grain orientations are present, so that single and multiple slips are both present in the deformation process. Figure 2 shows the case of a FCC polycrystal (Fig.2a) and the case of a HCP polycrystal (Fig.2b). For the second one, the number of slip planes is reduced, if compared to FCC material, so that other mechanisms may become active, like twinning, or intergranular damage.

Volume element as well as finite element simulations will be shown. A series of models have been built in the last twenty years, coming from two communities of research: the literature shows either "purely phenomenological" models, or "dislocation based" models. Due to the reduced space, it has been decided to promote the "operational" aspect of the models, so that the presentation will be focused on the phenomenological models. Nevertheless, a link will be made between the two approaches. The outline of the part is as follows:

- to be complete, a short introduction to thermodynamical approach is first given, and followed by the presentation of a class of crystal plasticity models;
- some applications of these models in finite element computations are then shown: this will concern first material identification and finite element computations of components or specimens, then some "microstructure computations", where single crystal models are used to represent individual grains in polycrystals;
- the last part is devoted to the applications of these models in uniform fields approaches, that may offer sometimes an interesting compromise between the macroscopic models and the full microstructure computations.

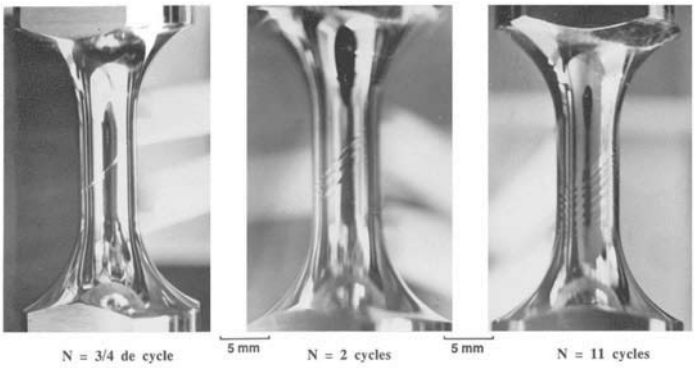

Figure 1. Slip system activity on a single crystalline specimen (Hanriot, 1993)

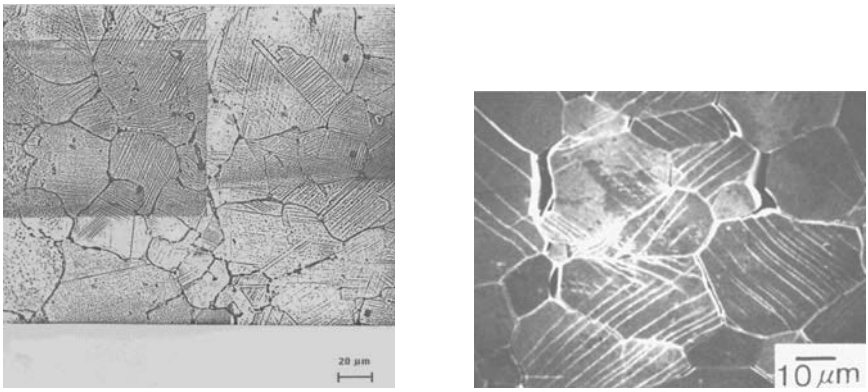

(a) (b)

Figure 2. Slip system activity in polycrystalline specimens: (a) waspaloy (Clavel, 1980), (b) zircaloy, with intergranular damage (Kubo et al., 1985)

2 A thermodynamical approach to single crystal plasticity

The thermodynamical framework Coleman (1964); Halphen and Nguyen (1975); Germain et al. (1983) is recalled for the general case of inelastic constitutive equations. The presentation is restricted to the case of small strains, since this is the typical deformation range used in the present document.

2.1 General framework

First and second principle. The first principle is the expression of the conservation of the energy. On a domain $\mathcal{D}$, the internal energy E, that is obtained by integrating the specific internal energy, e, is the sum of the power of the external forces and of the heat exchanges:

$$\frac{dE}{dt} = \int_{\mathcal{D}} \rho \frac{de}{dt} dV = \mathcal{P}^{(e)} + \dot{Q} \tag{1}$$

with the following definitions:

- Power of external forces:

$$\mathcal{P}^{(e)} = \int_{\mathcal{D}} \underset{\sim}{\boldsymbol{\sigma}} : \dot{\underset{\sim}{\boldsymbol{\varepsilon}}} dV \tag{2}$$

- Heat exchanged, using the rate of captured heat, $\underline{\boldsymbol{q}}$, and $\underline{\boldsymbol{n}}$, outside normal to the surface $\partial\mathcal{D}$, and r, volumetric heat:

$$\dot{Q} = \int_{\mathcal{D}} r dV - \int_{\partial\mathcal{D}} \underline{\boldsymbol{q}}.\underline{\boldsymbol{n}} dS = \int_{\mathcal{D}} (r - div\underline{\boldsymbol{q}})\, dV \tag{3}$$

This provides the following expression for the first principle:

$$\rho \frac{de}{dt} = \underset{\sim}{\boldsymbol{\sigma}} : \dot{\underset{\sim}{\boldsymbol{\varepsilon}}} + r - div\underline{\boldsymbol{q}} \tag{4}$$

The second principle provides an upper bound of the heat rate received by the volume $\mathcal{D}$ at a temperature T, and can be expressed as a function of the entropy S or of the specific entropy s :

$$\frac{dS}{dt} \geqslant \int_{\mathcal{D}} \frac{r}{T} dV - \int_{\partial\mathcal{D}} \frac{\underline{\boldsymbol{q}}.\underline{\boldsymbol{n}}}{T} dS \tag{5}$$

$$\text{then:} \qquad \int_{\mathcal{D}} \left(\rho \frac{ds}{dt} - \frac{r}{T} + div\left(\frac{\underline{\boldsymbol{q}}}{T}\right) \right) dV \geqslant 0 \tag{6}$$

Using Helmoltz free energy Ψ, such as $e = \Psi + Ts$, one get the so called *Clausius-Duhem* inequality:

$$\underset{\sim}{\boldsymbol{\sigma}} : \dot{\underset{\sim}{\boldsymbol{\varepsilon}}} - \rho\frac{d\Psi}{dt} - \rho s\dot{T} - \frac{1}{T}\underline{\boldsymbol{q}}.\underline{\boldsymbol{grad}}(T) \geqslant 0 \tag{7}$$

The *method of local state* assumes that the whole history of the material can be represented by the temperature T and by a set of *state variables* α_i, that are involved in Ψ, and which will be used in the classical Coleman–Noll argument. One successively get:

$$\frac{d\Psi}{dt} = \frac{\partial\Psi}{\partial T}\dot{T} + \frac{\partial\Psi}{\partial\alpha_i}\dot{\alpha}_i \tag{8}$$

$$s = -\frac{\partial\Psi}{\partial T} \tag{9}$$

$$\sigma_{ij}\dot{\varepsilon}_{ij} - \rho\,\frac{\partial\Psi}{\partial\alpha_i}\dot{\alpha}_i - \frac{1}{T}\,\underline{\boldsymbol{q}}\,.\,\underline{\boldsymbol{grad}}(T) \geqslant 0 \qquad (4) \tag{10}$$

The intrinsic dissipation Φ_1 and the thermal dissipation Φ_2 are considered:

$$\Phi_1 = \sigma_{ij}\dot{\varepsilon}_{ij} - \rho\frac{\partial\Psi}{\partial\alpha_i}\dot{\alpha}_i \qquad \Phi_2 = -\frac{1}{T}\,\underline{\boldsymbol{q}}\,.\,\underline{\boldsymbol{grad}}(T) \tag{11}$$

One assumes then that both of them must be positive. This is directly given by the Fourier's law, which provides the heat equation in presence of mechanical strain

$$\underline{\boldsymbol{q}} = -k(T,\alpha_i)\,\underline{\boldsymbol{grad}}(T) \tag{12}$$

$$div\left(k\,\underline{\boldsymbol{grad}}(T)\right) = \rho C_\varepsilon\dot{T} - r - \sigma_{ij}\dot{\varepsilon}_{ij} + \rho\left(\frac{\partial\Psi}{\partial\alpha_i} - T\frac{\partial^2\Psi}{\partial T\partial\alpha_i}\right)\dot{\alpha}_i \qquad (5) \tag{13}$$

(with $C_\varepsilon = T\partial s/\partial T$, specific heat at a constant strain) The shape of the mechanical part may take various forms, according to the type of material.

Thermoelasticity. The only internal variable is the elastic strain. Since elasticity is a non dissipative process, Φ_1 remains equal to zero. This provides a definition for the stress tensor:

$$\Phi_1 = \underset{\sim}{\boldsymbol{\sigma}} : \dot{\underset{\sim}{\boldsymbol{\varepsilon}}}^e - \rho\frac{\partial\Psi}{\partial\underset{\sim}{\boldsymbol{\varepsilon}}^e} : \dot{\underset{\sim}{\boldsymbol{\varepsilon}}}^e = 0 \tag{14}$$

These constitutive equations involve then two state variables, T and $\underset{\sim}{\boldsymbol{\varepsilon}}^e$, and two conjugated variables, the entropy s and the stress tensor $\underset{\sim}{\boldsymbol{\sigma}}$. Ψ can be seen as a *thermodynamic potential* which characterises reversible processes.

Dissipative processes. A series of hardening variables is now related to the list of the state variables α_I, so that the model is formulated according to the following scheme:

State variables		Conjugated variables	
temperature	T	$s = -\dfrac{\partial \Psi}{\partial T}$	entropy
elastic strain	$\underset{\sim}{\varepsilon}^e$	$\underset{\sim}{\sigma} = \rho \dfrac{\partial \Psi}{\partial \underset{\sim}{\varepsilon}^e}$	stress
state variables	α_I	$A_I = \rho \dfrac{\partial \Psi}{\partial \alpha_I}$	hardening variables

The intrinsic dissipation can be rewritten:

$$\Phi_1 = \underset{\sim}{\sigma} : \dot{\underset{\sim}{\varepsilon}}^p - A_I \dot{\alpha}_I = \mathrm{Z}\,\dot{\mathrm{z}} \tag{15}$$

with : $\mathrm{Z} = \{\underset{\sim}{\sigma}, A_I\}$; $\mathrm{z} = \left\{\underset{\sim}{\varepsilon}^p, -\alpha_I\right\}$

A model is *standard* (Halphen and Nguyen, 1975) if one can find a potential $\Omega \equiv \Omega(\mathrm{Z})$ such as:

$$\dot{\mathrm{z}} = \frac{\partial \Omega}{\partial \mathrm{Z}} \tag{16}$$

If Ω is a convex function of Z which includes the origin, the dissipation is then automatically positive, since:

$$\phi_1 = \mathrm{Z}\,\frac{\partial \Omega}{\partial \mathrm{Z}} \tag{17}$$

One can also define (through the Legendre-Fenchel transform) a companion potential in terms of $\dot{\mathrm{z}}$:

$$\Omega^*(\dot{\mathrm{z}}) = \max_{\mathrm{Z}} \left(\mathrm{Z}\,\dot{\mathrm{z}} - \Omega(\mathrm{Z})\right) \tag{18}$$

As a consequence, either $\Omega^*(\dot{\mathrm{z}})$ or $\Omega(\mathrm{Z})$ can be introduced to characterize the dissipative processes. A dissipative model can then be fully characterised by the definition of two potentials Ψ and Ω. The relation between state variables and hardening variables will then be derived from Ψ, and the nature of the hardening variables and their evolution rules from Ω. As an example, isotropic and nonlinear kinematic hardenings come from the following choice for the sets $(A_I,\ \alpha_I)$ is:

Type of hardening	State variable	Conjugated variable
Isotropic hardening	r	R
Kinematic hardening	$\underset{\sim}{\boldsymbol{\alpha}}$	$\underset{\sim}{\boldsymbol{X}}$

$$\dot{\underset{\sim}{\varepsilon}}^p = \frac{\partial \Omega}{\partial \underset{\sim}{\sigma}} \qquad \dot{r} = -\frac{\partial \Omega}{\partial R} \qquad \dot{\underset{\sim}{\alpha}} = -\frac{\partial \Omega}{\partial \underset{\sim}{X}} \tag{19}$$

Assuming that J is a von Mises norm, such as $J(\underset{\sim}{x}) = ((3/2)\underset{\sim}{x} : \underset{\sim}{x})^{1/2}$, a viscoplastic model is simply obtained by means of a potential Ω, according to the following steps:

- Definition of a viscoplastic yield:

$$f(\underset{\sim}{\sigma}, \underset{\sim}{X}, R) = J(\underset{\sim}{\sigma} - \underset{\sim}{X}) - R \tag{20}$$

- Definition of a potential, function of f:

$$\Omega = \frac{K}{n+1} \left(\frac{f}{K}\right)^{n+1} \tag{21}$$

- Viscoplastic flow:

$$\dot{\underset{\sim}{\varepsilon}}^p = \frac{\partial \Omega}{\partial \underset{\sim}{\sigma}} = \frac{\partial \Omega}{\partial f} \frac{\partial f}{\partial \underset{\sim}{\sigma}} \tag{22}$$

- Intensity of the flow (here, Norton with internal stress):

$$\dot{v} = \frac{\partial \Omega}{\partial f} = \left(\frac{f}{K}\right)^n \tag{23}$$

- Flow direction (normal to the yield surface):

$$\underset{\sim}{n} = \frac{\partial f}{\partial \underset{\sim}{\sigma}} \tag{24}$$

- Hardening:

$$\dot{r} = -\frac{\partial \Omega}{\partial R} \qquad \dot{\underset{\sim}{\alpha}} = -\frac{\partial \Omega}{\partial \underset{\sim}{X}} \tag{25}$$

One can switch from a viscoplastic to a time independent plastic model by replacing the viscoplastic potential by a plastic pseudo-potential, as shown in Fig.3, where Ind(f) jumps from 0 (for $f < 0$) to infinity (for $f = 0$). The strain rate is then no longer given by the partial derivative of Ω with respect to f, but by the consistency condition. The direction of the flow is recovered by introduction of *Hill's principle*, which assumes that the real stress field provides a maximum of the intrinsic dissipated power $\Phi_1 = \underset{\sim}{\sigma}^* : \dot{\underset{\sim}{\varepsilon}}^p$ of any admissible stress field, when there is no hardening:

$$\forall \underset{\sim}{\sigma}^* \text{ admissible } (\underset{\sim}{\sigma} - \underset{\sim}{\sigma}^*)\dot{\underset{\sim}{\varepsilon}}^p \geqslant 0 \tag{26}$$

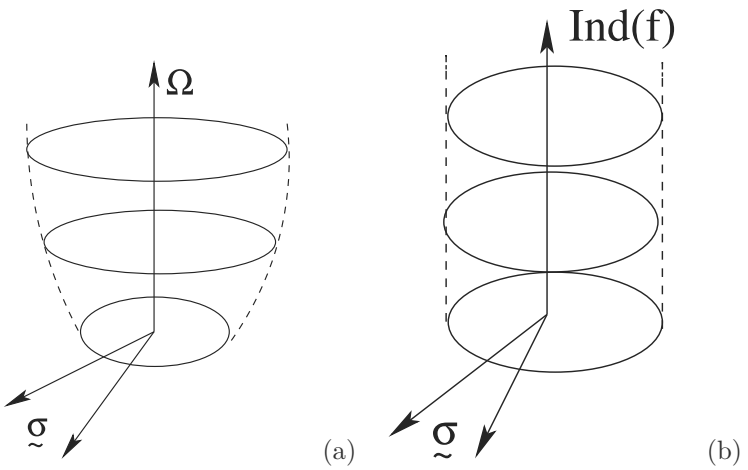

Figure 3. Illustration of (a) the viscoplastic potential, (b) the plastic pseudo-potential

For the case of a material with hardening, the preceding equation has to be reformulated as:

$$\Phi_1 = \underset{\sim}{\boldsymbol{\sigma}}^* : \dot{\underset{\sim}{\varepsilon}}^p - A_I^* \dot{\alpha}_I = \underset{\sim}{\boldsymbol{\sigma}} : \dot{\underset{\sim}{\varepsilon}}^p - \dot{\Psi}_p = \mathrm{Z}\ \dot{z} \qquad \text{maximum} \tag{27}$$

where Z includes stress and the hardening variables A_I, and z includes plastic strain and the state variables ($-\alpha_I$):

$$(\mathrm{Z} - \mathrm{Z}^*)\, \dot{z} \geqslant 0 \tag{28}$$

The maximization of Φ_1 *under the constraint* $f \leqslant 0$ can be seen as an extension of Hill's principle. Let us define $\mathbb{F}(\mathrm{Z}) = \mathrm{Z}\dot{z} - \dot{\lambda} f$ and search for the zero of $\partial\mathbb{F}/\partial\mathrm{Z}$

$$\dot{z} = \dot{\lambda} \frac{\partial f}{\partial \mathrm{Z}} \qquad \text{then:} \quad \dot{\underset{\sim}{\varepsilon}}^p = \dot{\lambda} \frac{\partial f}{\partial \underset{\sim}{\boldsymbol{\sigma}}} = \dot{\lambda}\, \underset{\sim}{\boldsymbol{n}} \qquad \dot{\alpha}_I = -\dot{\lambda} \frac{\partial f}{\partial A_I} \tag{29}$$

$\dot{\lambda}$ (at first unknown) plays in plasticity the rôle of the equivalent strain rate in viscoplasticity.

This type of approach offers the opportunity to introduce two types of coupling:

- *State coupling*, in the free energy (note the symmetry of the interactions):

$$\Psi(\alpha_1, \alpha_2) = \frac{1}{2} c_{11} \alpha_1^2 + \frac{1}{2} c_{22} \alpha_2^2 + \frac{1}{2} c_{12} \alpha_1 \alpha_2 \tag{30}$$

α_1 et α_2 :

$$\frac{\partial A_1}{\partial \alpha_2} = \frac{\partial A_2}{\partial \alpha_1} = \frac{\partial^2 \phi}{\partial \alpha_1 \partial \alpha_2} \tag{31}$$

- *Dissipative coupling*, when Ω is the sum of several potential functions, Ω_K:

$$\dot{z} = \sum_K \frac{\partial \Omega_K}{\partial Z} \tag{32}$$

More information about the development of specific models can be found in (Germain et al., 1983; Lemaitre and Chaboche, 1990; Besson et al., 1998).

2.2 Derivation of single crystal models

General framework The single crystal is seen as a collection of N slip systems, defined by their slip planes $\underline{\boldsymbol{n}}^s$ and slip direction $\underline{\boldsymbol{l}}^s$. The orientation tensor is:

$$\underset{\sim}{\boldsymbol{m}}^s = \frac{1}{2}(\underline{\boldsymbol{n}}^s \otimes \underline{\boldsymbol{l}}^s + \underline{\boldsymbol{l}}^s \otimes \underline{\boldsymbol{n}}^s) \tag{33}$$

In small perturbation, the resolved shear stress is computed as

$$\tau^s = \underset{\sim}{\boldsymbol{\sigma}} : \underset{\sim}{\boldsymbol{m}}^s \tag{34}$$

and the strain partition involves an elastic and an inelastic strain

$$\dot{\underset{\sim}{\varepsilon}} = \dot{\underset{\sim}{\varepsilon}}^e + \dot{\underset{\sim}{\varepsilon}}^p \tag{35}$$

The elasticity is characterized as usual, meanwhile dissipative behaviour must be expressed for each slip system. As a consequence, isotropic and kinematic variables have to be defined on each slip system. The resulting set of variables is then as follows:

Phenomenon	State variable	Associated variable
Elasticity	$\underset{\sim}{\boldsymbol{\varepsilon}}^e$	$\underset{\sim}{\boldsymbol{\sigma}}$
Isotropic hardening	ρ^s, $s = 1..N$	r^s, $s = 1..N$
Kinematic hardening	α^s, $s = 1..N$	x^s, $s = 1..N$

The relation between state and associated variables comes from free energy, where the elastic and the inelastic part are assumed to be disconnected:

$$\rho\psi(\underset{\sim}{\boldsymbol{\varepsilon}}^e, \rho^s, \alpha^s) = \rho\psi^e(\underset{\sim}{\boldsymbol{\varepsilon}}^e) + \rho\psi^p(\rho^s, \alpha^s) \tag{36}$$

The elasticity (non–dissipative process) is fully defined by

$$\rho\psi^e = \frac{1}{2}\,\underset{\sim}{\varepsilon}^e : \underset{\approx}{\mathbf{\Lambda}} : \underset{\sim}{\varepsilon}^e \tag{37}$$

The state variables α^s and ρ^s are present in the free energy, and the hardening variables x^s and r^s are defined as their partial derivatives:

$$\rho\psi^p = \frac{1}{2}\,c\sum_s (\alpha^s)^2 + \frac{1}{2}\,Q\sum_r\sum_s h_{rs}\rho^r\rho^s \tag{38}$$

$$x^r = c\alpha^r \quad ; \quad r^r = b\,Q\sum_s h_{rs}\rho^s \tag{39}$$

Note the *interaction matrix*, whose components h_{rs} characterize self–hardening (if $r = s$) and cross–hardening (if $r \neq s$). The multi-mechanism effect has been studied in detail in the past (Koiter, 1960; Mandel, 1965) from a theoritical point of view. Experimental aspects will be discussed later.

Viscoplasticity needs the definition of a viscoplastic potential, plasticity needs the definition of a plastic pseudopotential. They are built using the expression of the yield criterion on each slip system

$$f^s = |\tau^s - x^s| - r^s - \tau_0 \tag{40}$$

Viscoplastic formulation A viscoplastic potential is introduced. As an example, a power function of the yield is chosen here, but any other increasing function would be a good candidate:

$$\Omega = \sum_r \Omega_r(f^r) = \frac{K}{n+1}\sum_r \left\langle \frac{f^r}{K} \right\rangle^{n+1} \tag{41}$$

The viscoplastic flow can then be derived as

$$\dot{\underset{\sim}{\varepsilon}}^p = \frac{\partial\Omega}{\partial\underset{\sim}{\boldsymbol{\sigma}}} = \sum_r \frac{\partial\Omega_r}{\partial\underset{\sim}{\boldsymbol{\sigma}}} = \sum_r \frac{\partial\Omega_r}{\partial f^r}\,\frac{\partial f^r}{\partial\underset{\sim}{\boldsymbol{\sigma}}} = \sum_r \dot{v}^r\underset{\sim}{\boldsymbol{m}}^r\eta^r = \sum_r \dot{\gamma}^r\underset{\sim}{\boldsymbol{m}}^r \tag{42}$$

In the preceding equation, η^r stand for $sign(\tau^r - x^r)$; the scalar part of the expression characterises the viscoplastic shear rate:

$$\frac{\partial\Omega}{\partial f^r} = \left\langle \frac{f^r}{K} \right\rangle^n = \dot{v}^r \qquad \dot{\gamma}^r = \dot{v}^r sign(\tau^r - x^r) = \dot{v}^r\eta^r \tag{43}$$

and the tensorial part the flow direction, given by the normality rule:

$$\frac{\partial f^r}{\partial\underset{\sim}{\boldsymbol{\sigma}}} = \frac{\partial(|\underset{\sim}{\boldsymbol{m}}^r : \underset{\sim}{\boldsymbol{\sigma}} - x^r| - r^r - \tau_0)}{\partial\underset{\sim}{\boldsymbol{\sigma}}} = \underset{\sim}{\boldsymbol{m}}^r\eta^r \tag{44}$$

For a standard model, the variables attached to isotropic and kinematic hardenings are imposed:

- Kinematic hardening on system s is driven by the actual slip on this system, γ^s

$$\dot{\alpha}^s = -\frac{\partial \Omega}{\partial x^s} = -\sum_r \frac{\partial \Omega_r}{\partial x^s} = -\frac{\partial \Omega_s}{\partial f^s}\frac{\partial f^s}{\partial x^s} = \dot{v}^s \eta^s = \dot{\gamma}^s \tag{45}$$

- Isotropic hardening on system s is driven by the *accumulated slip* on this system, v^s:

$$\dot{\rho}^s = -\frac{\partial \Omega}{\partial r^s} = -\sum_r \frac{\partial \Omega_r}{\partial r^s} = -\frac{\partial \Omega_s}{\partial f^s}\frac{\partial f^s}{\partial r^s} = \dot{v}^s \tag{46}$$

Non standard models can also be defined:

$$\dot{\alpha}^s = (\eta^s - d\alpha^s)\dot{v}^s \tag{47}$$

$$\dot{\rho}^s = (1 - b\rho^s)\dot{v}^s \tag{48}$$

Since $\underset{\sim}{\boldsymbol{\sigma}} : \dot{\underset{\sim}{\varepsilon}}^p = \underset{\sim}{\boldsymbol{\sigma}} : \sum_s \underset{\sim}{\boldsymbol{m}}^s \dot{\gamma}^s = \sum_s \underset{\sim}{\boldsymbol{\sigma}} : \underset{\sim}{\boldsymbol{m}}^s \dot{\gamma}^s = \sum_s \tau^s \dot{\gamma}^s = \sum_s \tau^s \eta^s \dot{v}^s$ the intrinsic dissipation writes:

$$\phi_1 = \underset{\sim}{\boldsymbol{\sigma}} : \dot{\underset{\sim}{\varepsilon}}^p - \sum_s x^s \dot{\alpha}^s - \sum_s r^s \dot{\rho}^s \tag{49}$$

$$= \sum_s (\tau^s \eta^s \dot{v}^s - x^s(\eta^s - d\alpha^s)\dot{v}^s - r^s(1 - b\rho^s)\dot{v}^s) \tag{50}$$

$$= \sum_s (f^s + \tau_0 + \frac{d}{c}\,(x^s)^2 + br^s\rho^s)\dot{v}^s \tag{51}$$

The following contributions are then exhibited:

- Viscous dissipation : $\sum_s f^s \dot{v}^s$
- Friction dissipation : $\tau_0 \sum_s \dot{v}^s$
- Dissipation due to nonlinear hardening: $\left(\frac{d}{c}\,(x^s)^2 + br^s\rho^s\right)\dot{v}^s$

Plastic formulation. Figure 4 illustrates the difference between viscoplastic and plastic formulation. Like for the classical case (Fig.3), the current state in the stress space must stay on the yield surface instead of being on an equipotential. The plastic strain rate for each slip system is no

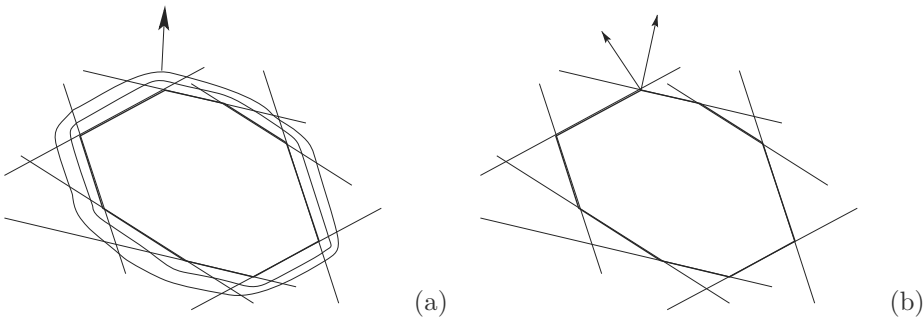

Figure 4. Illustration of (a) the viscoplastic flow, (b) the plastic flow

longer defined by the distance to the relevant yield, but must be deduced from the consistency condition. The regularisation provided by the viscous effect is no longer present, and the direction of the flow has to be defined by additional rules when the current point is on a corner of the domain, that is in situation of multiple slip. The crucial point is then to determine the set of active slip systems. One plastic multiplyier is determined for each slip system. The non zero plastic multiplyiers are solutions of the linear system formed by the consistency conditions on the active slip systems, $\dot{f}^s = 0$. Several sets of slip systems can produce the same viscoplastic strain rate tensor. An additional condition must be used to select the relevant set of slips, as discussed in section (2.5).

$$\underset{\sim}{\dot{\varepsilon}}^p = \sum_{s=1}^{N} \dot{\lambda}^s \frac{\partial f^s}{\partial \underset{\sim}{\boldsymbol{\sigma}}} = \sum_{s=1}^{N} \dot{\lambda}^s \underset{\sim}{\boldsymbol{m}}^s \tag{52}$$

A rather simple computation allows to obtain the relevant system, starting from:

- the strain partition

$$\dot{\underset{\sim}{\boldsymbol{\sigma}}} = \underset{\approx}{\boldsymbol{\Lambda}} : \left(\dot{\underset{\sim}{\boldsymbol{\varepsilon}}} - \sum_r \underset{\sim}{\boldsymbol{m}}^r \dot{\gamma}^r \right) \tag{53}$$

- the consistency condition applied to active slip systems:

$$f^s = |\underset{\sim}{\boldsymbol{m}}^s : \underset{\sim}{\boldsymbol{\sigma}} - x^s| - r^s - \tau_0 = 0 \qquad 0 = \underset{\sim}{\boldsymbol{m}}^s : \dot{\underset{\sim}{\boldsymbol{\sigma}}} - \dot{x}^s - \eta^s \dot{r}^s \tag{54}$$

using the notation $\eta^s = sign(\tau^s - x^s)$

The following step consists in computing $\underset{\sim}{\boldsymbol{m}}^s : \dot{\underset{\sim}{\boldsymbol{\sigma}}}$ in equation (54), introducing H_{sr}, as specified below, and keeping the notation $\dot{v}^s$ for the plastic shear strain rate on system r:

$$\underset{\sim}{\boldsymbol{m}}^s : \dot{\underset{\sim}{\boldsymbol{\sigma}}} = \dot{x}^s + \eta^s \dot{r}^s = \sum_r H_{sr} \dot{v}^r \tag{55}$$

In the next step, one replaces $\dot{\underset{\sim}{\boldsymbol{\sigma}}}$ by its expression in equation (53):

$$\underset{\sim}{\boldsymbol{m}}^s : \underset{\approx}{\boldsymbol{\Lambda}} : \dot{\underset{\sim}{\boldsymbol{\varepsilon}}} - \sum_r \underset{\sim}{\boldsymbol{m}}^s : \underset{\approx}{\boldsymbol{\Lambda}} : \underset{\sim}{\boldsymbol{m}}^r \eta^r \dot{v}^r = \sum_r H_{sr} \dot{v}^r \tag{56}$$

Under prescribed strain rate, N equations are then defined (N = number of active slip systems) to compute the plastic multiplyiers:

$$\sum_r \left(\underset{\sim}{\boldsymbol{m}}^s : \underset{\approx}{\boldsymbol{\Lambda}} : \underset{\sim}{\boldsymbol{m}}^r + H_{sr} \right) \dot{v}^r = \underset{\sim}{\boldsymbol{m}}^s : \underset{\approx}{\boldsymbol{\Lambda}} : \dot{\underset{\approx}{\boldsymbol{\varepsilon}}} \tag{57}$$

- The set of possible slip systems able to respect these equations is not unique. Several combinations of slip can provide the same macroscopic strain rate. This point will be examined later in section (2.5).
- Note that, in the present model, the matrix formed by the coefficients H_{sr} is non symmetric:

$$\dot{x}^s = c\dot{\gamma}^s - dx^s \dot{v}^s = (c\eta^s - dx^s)\dot{v}^s = \sum_r (c\eta^r - dx^r)\delta_{rs}\dot{v}^r \tag{58}$$

$$\dot{r}^s = Q \sum_r bh_{sr} \exp(-bv^r)\dot{v}^r \tag{59}$$

$$H_{sr} = (c\eta^r - dx^r)\delta_{sr} + Qbh_{sr} \exp(-bv^r) \tag{60}$$

Nevertheless, it becomes symmetric with no kinematic hardening and linear isotropic hardening, $r^s = \sum_r h_{sr} v^r$

$$H_{sr} = h_{sr} \tag{61}$$

- The following double dot products may be useful in the computations:

$$\underset{\sim}{\boldsymbol{m}}^s : \underset{\sim}{\boldsymbol{I}} = m^s_{ij}\delta_{ij} = \mathrm{trace}(\underset{\sim}{\boldsymbol{m}}^{\boldsymbol{s}}) = m^s_{ii} = n^s_i l^s_i = 0 \tag{62}$$

$$\underset{\sim}{\boldsymbol{m}}^s : \underset{\sim}{\boldsymbol{m}}^s = m^s_{ij} m^s_{ij} = \frac{1}{4}(n^s_i l^s_j + l^s_i n^s_j)(n^s_i l^s_j + l^s_i n^s_j) = \frac{1}{2} \tag{63}$$

$$\underset{\sim}{\boldsymbol{m}}^s : \underset{\sim}{\boldsymbol{m}}^r = m^s_{ij} m^r_{ij} = \frac{1}{4}(n^r_i l^r_j + l^r_i n^r_j)(n^s_i l^s_j + l^s_i n^s_j) \tag{64}$$

Table 1. The components of the 12 orientation tensors for octahedral slip systems

num syst	1	2	3	4	5	6	7	8	9	10	11	12
$\sqrt{6}m_{11}$	-1	0	-1	-1	0	1	0	-1	-1	-1	1	0
$\sqrt{6}m_{22}$	0	-1	1	0	-1	-1	-1	1	0	1	0	1
$\sqrt{6}m_{33}$	1	1	0	1	1	0	1	0	1	0	-1	-1
$2\sqrt{6}m_{12}$	-1	-1	0	1	1	0	1	0	1	0	1	1
$2\sqrt{6}m_{23}$	1	0	1	-1	0	1	0	1	1	-1	1	0
$2\sqrt{6}m_{31}$	0	1	-1	0	1	1	-1	1	0	1	0	1

- For the case of isotropic elasticity, the system (57) can be simplified, since

$$\Lambda_{ijkl} = \lambda\delta_{ij}\delta_{kl} + \mu(\delta_{ik}\delta_{jl} + \delta_{il}\delta_{jk}) \tag{65}$$

$$\Lambda_{ijkl}m^r_{kl} = \mu m^r_{ij} \tag{66}$$

$$\underset{\sim}{\boldsymbol{m}}^s : \underset{\approx}{\boldsymbol{\Lambda}} : \underset{\sim}{\boldsymbol{m}}^r = \mu m^s_{ij} m^r_{ij} \tag{67}$$

$$\tag{68}$$

2.3 Yield surfaces

Yield surfaces provide a synthetic information on the behaviour of the materials. This is illustrated here for the simple case of FCC materials, where slip occurs on the four octahedral planes $\{111\}$, in the directions $\langle 110\rangle$. The case of Ni-Base superalloys, where cubic planes $\{001\}$ may also be involved, with the same slip directions $\langle 110\rangle$, will be also mentioned.

The yield surfaces can be seen as a collection of hyperplans which equations are:

$$|\tau^s| - \tau_c = 0 \quad \text{or} \quad \underset{\sim}{\boldsymbol{\sigma}} : \underset{\sim}{\boldsymbol{m}}^s - \tau_c = 0 \tag{69}$$

Plastic deformation of FCC materials classically involves the 12 octahedral slip systems only. The components of the 12 orientation tensors are shown in Table 1.

The shape of the yield loci can be illustrated on planes like biaxial or tension–shear loading:

- If the only non zero terms of the stress tensor are σ_{11} and σ_{22}, the criterion writes:

$$|\sigma_{11}m_{11} + \sigma_{22}m_{22}| - \tau_c = 0 \tag{70}$$

Table 2. Values of τ^s for the 12 slip systems of a FCC single crystal

(a) *case of a biaxial tension loading* σ_{11}–σ_{22}

num syst	1	2	3	4	5	6
τ^s	$-\sigma_{11}+\sigma_{22}$	σ_{22}	$-\sigma_{11}$	$-\sigma_{11}+\sigma_{22}$	σ_{22}	σ_{11}
num syst	7	8	9	10	11	12
τ^s	σ_{22}	$-\sigma_{11}$	$-\sigma_{11}+\sigma_{22}$	$-\sigma_{11}$	$\sigma_{11}-\sigma_{22}$	$-\sigma_{22}$

(b) *case of a tension–shear loading* σ_{11}–σ_{12}

num syst	1	2	3	4	5	6
τ^s	$-\sigma_{11}-\sigma_{12}$	$-\sigma_{12}$	$-\sigma_{11}$	$-\sigma_{11}+\sigma_{12}$	σ_{12}	σ_{11}
num syst	7	8	9	10	11	12
τ^s	σ_{12}	$-\sigma_{11}$	$-\sigma_{11}+\sigma_{12}$	$-\sigma_{11}$	$\sigma_{11}+\sigma_{12}$	σ_{12}

The resulting equations for the 12 slip systems are shown in Table 2a.

- If the only non zero terms of the stress tensor are σ_{11}, σ_{12} and σ_{21}, the criterion writes:

$$|\sigma_{11}m_{11}+2\sigma_{12}m_{12}|-\tau_c=0 \tag{71}$$

The resulting equations for the 12 slip systems are shown in Table 2b.

As a result, for biaxial tension loading, the domain is then defined by three types of systems :

- systems 1, 4, 9 and 11 : $|\sigma_{11}-\sigma_{22}|=\tau_c\sqrt{6}$
- systems 3, 6, 8, 10 : $|\sigma_{11}|=\tau_c\sqrt{6}$
- systems 2, 5, 7, 13 : $|\sigma_{22}|=\tau_c\sqrt{6}$

meanwhile two types of systems are present for tension–shear loading, as illustrated in Fig.5:

- systems 1 and 11 give : $|\sigma_{11}+\sigma_{12}|=\tau_c\sqrt{6}$
- systems 4 and 9 give : $|\sigma_{11}-\sigma_{12}|=\tau_c\sqrt{6}$

Figure 5 illustrates also the influence of the hardening matrix. It is assumed that the current loading point is at the corner located located on the σ_{12} axis, for a positive value of the resolved shear stress. A stress increment is applied, with an angle θ with the horizontal at this point. Numbers in Fig.5a indicate the number of active slip systems if the interaction matrix is diagonal. On the other hand, if cross hardening (the terms outside of the diagonal) is high, slip on systems like 1 or 11 may dramatically increase the

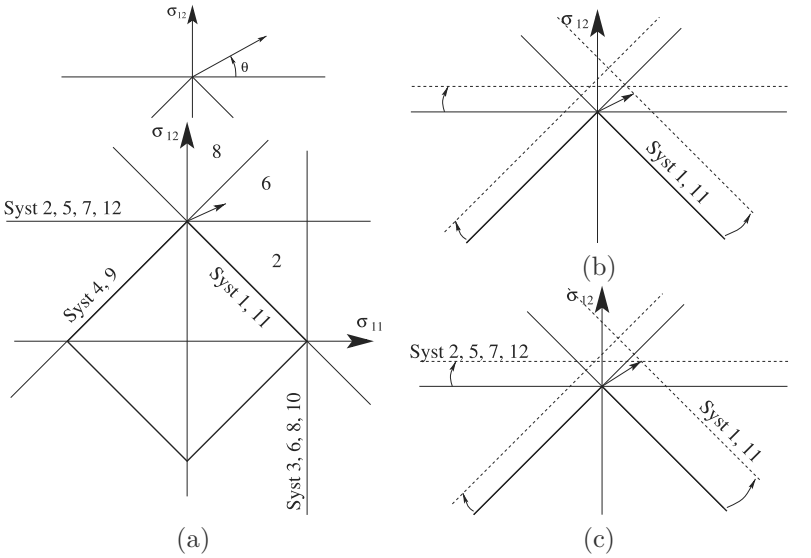

Figure 5. Graphical illustration of the slip system activation: (a) number of potentially active slip systems for various load directions, (b) high latent hardening, a few active systems, (c) low latent hardening, many active systems

resolved shear stress on systems like 2, 5,... so that they will not become active, even if the stress increment is in the sector indicated (6), as demonstrated by Fig.5b. An intermediate solution is recovered for intermediate values of the cross hardening terms (Fig.5c).

Multiple slip is often present in single crystal. This might be due to the rotation of the slip planes during the deformation process. On the other hand, this is also a character which is related to the balance between elastic and plastic flow direction. For instance, in Fig.6a, two loading paths under prescribed strain are considered: for the upper path, the ratio $\varepsilon_{12}^{max}/\varepsilon_{11}^{max}$ is equal to 0.525, for the lower path, the same ratio is equal to 0.475. Since the ratio $\varepsilon_{12}^{pmax}/\varepsilon_{11}^{pmax}$ remains always equal to 0.5, there is a continuous deviation for the stress rate which explains the shape of the stress path. The same argument is valid for explaining the stress path in Fig.6b. Note that in Fig.6a, systems like 2, 5, 7, 12 start being active due to the loading deviation for the upper path, and systems 3, 6, 8, 10 for the lower path.

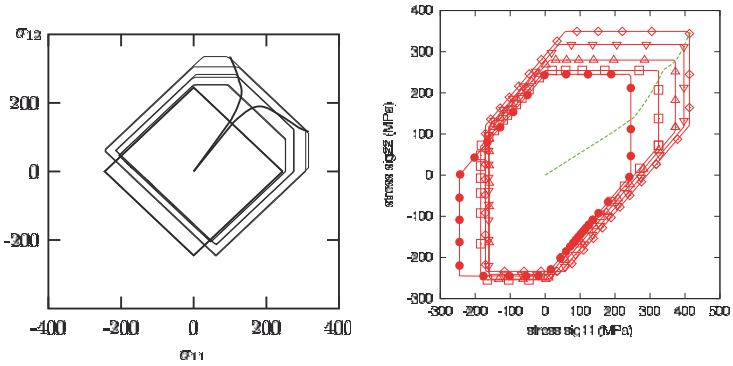

Figure 6. Initial and subsequent yield surfaces: (a) for tension–shear stress states, (b) for biaxial stress states

2.4 Identification under tension and tension–shear loadings

For a given crystal orientation, the present model can be compared with a macroscopic model. Its identification can then be made either by curve fitting using tensile curves, or by a direct use of the material parameters of a macroscopic model. Examples of such an approach can be found in (Méric et al., 1991; Hanriot et al., 1991) for superalloy single crystals. For the case of multiple slip, with N equivalent slip systems, and a Schmid factor m, one can transform the general expression giving $\dot{\underset{\sim}{\varepsilon}}^p$:

$$\dot{\underset{\sim}{\varepsilon}}^p = \sum_s \underset{\sim}{\boldsymbol{m}}^s \dot{v}^s = \sum_s \underset{\sim}{\boldsymbol{m}}^s \left\langle \frac{|\tau^s - x^s| - r^s}{k} \right\rangle^n \tag{72}$$

$$= Nm \left\langle \frac{m(\sigma - x) - r}{k} \right\rangle^n \tag{73}$$

which can be compared to a macroscopic model

$$\dot{\varepsilon}^p = \left\langle \frac{(\sigma - X) - R}{K} \right\rangle^n \text{ with } K = \frac{k}{m} \frac{1}{mN}^{1/n} \quad X = \frac{x}{m} \quad R = \frac{r}{m} \tag{74}$$

The relations between the macroscopic material parameters and the parameters of the crystalline models are given in Table 3 for the case of octahedral slip and cube slip.

Two examples are given, in order to illustrate the various types of mechanical response of the mode. Figure 7 simply shows the tensile curves

Table 3. Relation between the material parameters of macroscopic models and of crystal plassticity models for octahedral slip and cube slip.

Coefficient	Value for multiple slip (m,M)	Value for 001 tension $N = 8$, $m = 1/\sqrt{6}$	Value for 111 tension $N = 6$, $m = \sqrt{2}/3$
K	$\frac{k}{m(Mm)^{1/n}}$	$\frac{\sqrt{6}k}{(8/\sqrt{6})^{1/n}}$	$\frac{3k}{2^{(n+1)/2n}}$
R_0	$\frac{r_o}{m}$	$\sqrt{6}r_o$	$\frac{3r_o}{\sqrt{2}}$
Q	$\frac{Q}{m}$	$\sqrt{6}Q$	$\frac{3Q}{\sqrt{2}}$
b	$\frac{b}{mM}$	$\frac{\sqrt{6}b}{8}$	$\frac{b}{\sqrt{2}}$
C	$\frac{c}{Mm^2}$	$\frac{3c}{4}$	$\frac{3c}{2}$
D	$\frac{d}{Mm}$	$\frac{\sqrt{6}d}{8}$	$\frac{d}{\sqrt{2}}$

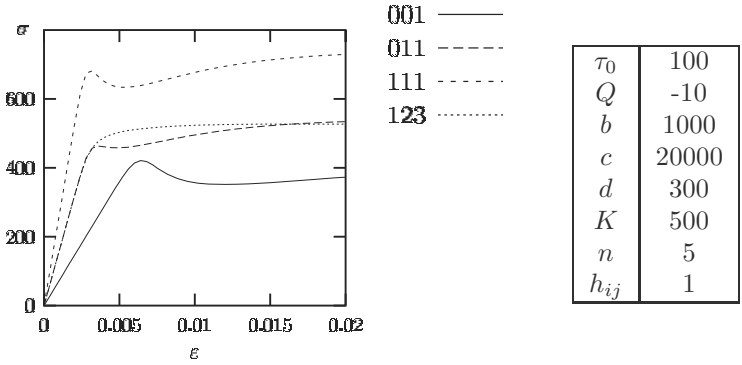

τ_0	100
Q	-10
b	1000
c	20000
d	300
K	500
n	5
h_{ij}	1

Figure 7. Simulation of the tensile behaviour for various crystallographic orientations

obtained with a negative value of the material parameter Q for isotropic hardening. Figure 8 is the result of the identification of the model on an experimental data base obtained on AM1 for various crystal orientations (Hanriot et al., 1991).

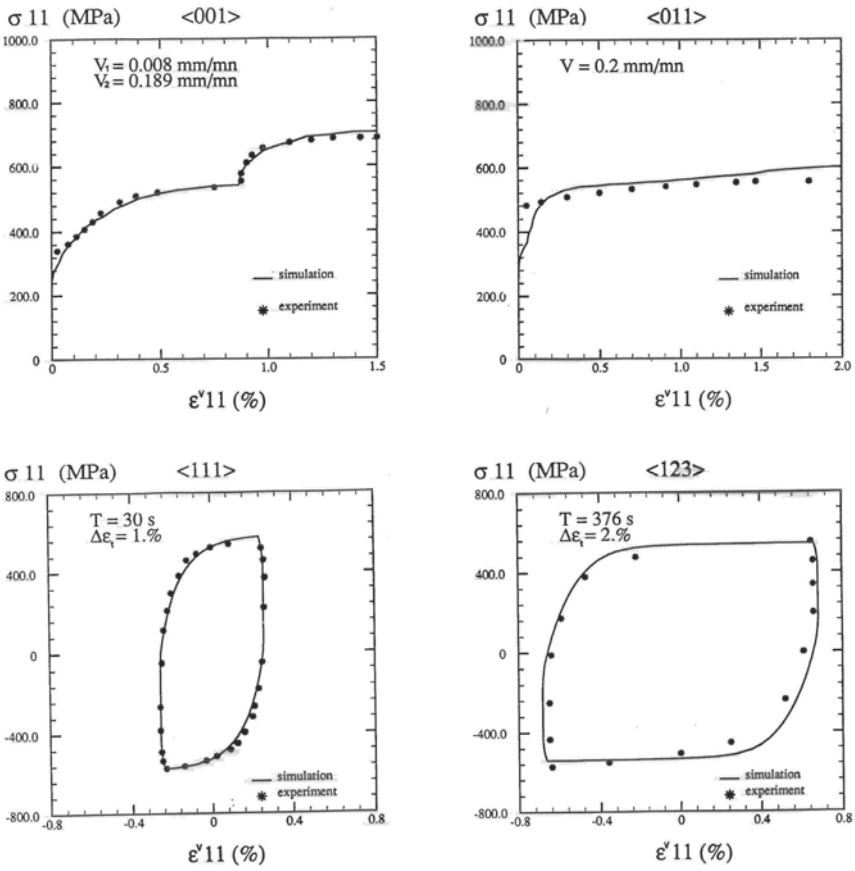

Figure 8. Simulation of the cyclic behaviour for various crystallographic orientations on AM1 specimens (Hanriot et al., 1991)

2.5 Slip system selection

As previously pointed out (section 2.2), there is no unique set of slip systems that provides a given plastic strain rate tensor. The condition to fullfil for each set of slip systems to be admissible can be precised by means of the variational approach, using either internal or external power.

The first problem is to select a set of admissible shear rates $\dot{v}^s$ for a prescribed plastic strain rate $\dot{\underset{\sim}{\varepsilon}}^p$ (assuming $\underset{\sim}{\varepsilon} \equiv \underset{\sim}{\varepsilon}^p$). This has to be done by minimising the internal power of the material element (Taylor, 1938):

$$\mathcal{P}_i = \sum_s \tau_c^s \dot{v}^s \tag{75}$$

the shear strain rates being submitted to the constraint:

$$\underset{\sim}{\boldsymbol{g}}(\dot{v}^s) = \dot{\underset{\sim}{\varepsilon}}^p - \sum_s \underset{\sim}{\boldsymbol{m}}^s \dot{v}^s \eta^s = 0 \tag{76}$$

Let us define the lagrangian $\mathcal{F}_i$, and search for the saddle point

$$\mathcal{F}_i\left(\dot{v}^s, \underset{\sim}{\boldsymbol{\lambda}}\right) = \mathcal{P}_i + \underset{\sim}{\boldsymbol{\lambda}} : \underset{\sim}{\boldsymbol{g}} \tag{77}$$

$$\frac{\partial \mathcal{F}_i}{\partial \underset{\sim}{\boldsymbol{\lambda}}} = \dot{\underset{\sim}{\varepsilon}}^p - \sum_s \underset{\sim}{\boldsymbol{m}}^s \dot{v}^s = 0 \qquad \frac{\partial \mathcal{F}_i}{\partial \dot{v}^s} = \tau_c^s - \underset{\sim}{\boldsymbol{\lambda}} : \underset{\sim}{\boldsymbol{m}}^s \eta^s = 0 \tag{78}$$

The tensor $\underset{\sim}{\boldsymbol{\lambda}}$ is nothing but the stress tensor. To find the set of shear strain rates, which minimizes internal power, it is then necessary to find a stress tensor which obeys the yield conditions, *id est* which allows to build resolved shear stresses that reach τ_c^s on the active slip systems and that are smaller than τ_c^s on the inactive ones.

The problem can also be posed in terms of unknown stress, and rephrased as "find the stress state which maximise the external power" (Bishop and Hill, 1951), written as

$$\mathcal{P}_e = \underset{\sim}{\boldsymbol{\sigma}} : \dot{\underset{\sim}{\varepsilon}}^p \tag{79}$$

under the constraint

$$g^s(\underset{\sim}{\boldsymbol{\sigma}}) = \tau_c^s - \underset{\sim}{\boldsymbol{\sigma}} : \underset{\sim}{\boldsymbol{m}}^s \geqslant 0 \tag{80}$$

The lagrangian function is then now:

$$\mathcal{F}_e(\underset{\sim}{\boldsymbol{\sigma}}, \dot{\mu}^s) = \mathcal{P}_e + \sum_s \dot{\mu}^s g^s \tag{81}$$

$$\frac{\partial \mathcal{F}_e}{\partial \underset{\sim}{\boldsymbol{\sigma}}} = \dot{\underset{\sim}{\varepsilon}}^p - \sum_s \underset{\sim}{\boldsymbol{m}}^s \dot{\mu}^s = 0 \qquad \frac{\partial \mathcal{F}_e}{\partial \dot{\mu}^s} = \tau_c^s - \underset{\sim}{\boldsymbol{\sigma}} : \underset{\sim}{\boldsymbol{m}}^s = 0 \tag{82}$$

The multiplyiers $\dot{\mu}^s$ are nothing but plastic strain rates. To find a stress tensor, one has to find a set of plastic shear strain rates which are zero on the inactive slip systems, and positive on the active slip systems.

The two approaches can be summarised by the double inequality

$$\underset{\sim}{\boldsymbol{\sigma}}^* : \dot{\underset{\sim}{\varepsilon}}^p \leqslant \underset{\sim}{\boldsymbol{\sigma}} : \dot{\underset{\sim}{\varepsilon}}^p = \sum_s \tau_c^s \dot{v}^s \leqslant \sum_s \tau_c^s \dot{v}'^s \tag{83}$$

This discussion can be found in (Chin and Mammel, 1969). It means that:

- between all the admissible stress states conjugated to the real plastic strain rate, the real stress tensor maximises the plastic power. For regular points of the yield surface, this ensures that the plastic strain rate is normal to the yield surface. Nevertheless, this does not provide the full information for a corner of the yield surface, in conditions of multislip;
- between all the possible set of viscoplastic shear strain rates, the real one minimizes the internal power.

The dissipation computed in the thermodynamical approach for such a simple model has two terms only:

$$\Phi_1 = \underset{\sim}{\boldsymbol{\sigma}} : \dot{\underset{\sim}{\varepsilon}}^p - \sum_s r^s \dot{v}^s \tag{84}$$

where the variables r^s, defined in equation (59), denote the *increase* of critical resolved shear stress. According to equation (40) (with $x^s = 0$, since there is no kinematic hardening here), if all the systems are equivalent, the equation can be reduced:

$$\Phi_1 = \sum_s \tau_0^s \dot{v}^s = \tau_0 \sum_s \dot{v}^s \tag{85}$$

2.6 Other crystal plasticity models

The model which has been considered up to now represents the branch of the phenomenological single crystal models, inspired from the macroscopic formulations, like also for instance (Jordan and Walker, 1985). An other class of models is represented by the so called *dislocation based models*, like for instance (Busso and McClintock, 1996). On the other hand, crystal plasticity is a versatile solution to express various phenomena acting on the level of the crystal network, like twinning. These two topics are shown in the present section. Additional capabilities will be shown later, namely developments needed to represent volume changes and damage.

Phenomenological and dislocation based models. We refer to the first denomination when the hardening variables are plastic slip, and to the second one when the dislocation mechanisms are explicitely introduced. One has to get back to Taylor (Taylor, 1938) to read the expression of the first phenomenological model, which assumes that the critical resolved shear stress on the slip systems linearly depend on the slips on all the systems, by means of the interaction matrix. The so called *Taylor interaction* is obtained when all the terms of the matrix are equal to 1: self-hardening and cross-hardening are exactly equivalent. Experimental measurement of cross hardening have then allowed to reach better estimations of the hardening matrix (Kocks and Brown, 1966; Kocks, 1970; Franciosi, 1985a,b). This matrix is now estimated by means of Dislocation Dynamics computations (Devincre et al., 2006). The most widely used phenomenological model is written in a viscoplastic framework without threshold (Asaro, 1983b), so that all the systems are allways active. A multiplicative isotropic hardening is introduced; it depends on accumulated slip:

$$\dot{\gamma}^s = \dot{\gamma}_0 \left(\frac{\tau^s}{\tau_c^s} \right)^{1/m} \tag{86}$$

$$\tau_c^s = \sum_{r=1}^{N} h_{sr} \gamma^r \tag{87}$$

$$\tag{88}$$

The phenomenological models previously presented in this paper and the dislocations based models have the same nature: their variables globally represent averages of the local dislocation densities. To fully illustrate this point, one can take (equations 89–91) the example of a dislocation based model (Tabourot et al., 1997), where b is the Burgers vector, and ρ^s the dislocation density on slip system s:

$$\dot{\gamma}^s = \dot{\gamma}_0 \left(\frac{\tau^s}{\tau_\mu^s} \right)^{1/m} \tag{89}$$

$$\tau_\mu^s = \alpha \mu b \left(\sum_{r=1}^{N} h_{sr} \rho^r \right)^{1/2} \tag{90}$$

$$\dot{\rho}^s = \frac{1}{b} \left(\frac{\left(\sum_{r=1}^{N} a^{sr} \rho^r \right)^{1/2}}{K} - 2 y_c \rho^s \right) \dot{\gamma}^s \tag{91}$$

After choosing $r^s = b^2\rho^s$ and $y_c = bk_c$, the last two equations can be rewritten:

$$\tau_\mu^s = \alpha\mu \left(\sum_{r=1}^{N} h_{sr} r^r \right)^{1/2} \tag{92}$$

$$\dot{r}^s = \left(\frac{\left(\sum_{r=1}^{N} a^{sr} r^r \right)^{1/2}}{K} - 2k_c r^s \right) \dot{\gamma}^s \tag{93}$$

The variable r^s which is defined here plays exactly the role of ρ^s in equations (38) and (48).

Twinning and phase transformation Twinning and martensitic transformation can be represented in a local frame $\underline{\boldsymbol{n}}^k$, $\underline{\boldsymbol{t}}^k$,$\underline{\boldsymbol{u}}^k$ by a transformation gradient F^k

$$F = I + \underline{\boldsymbol{t}^k} \otimes \underline{\boldsymbol{n}^k} \tag{94}$$

The stress-free transformation tensor is then $\frac{1}{2}\left(F^T F - I\right)$ in large strain, or $\frac{1}{2}\left(F^T + F\right) - I$ in a small perturbation framework. In this last case, the transformation of the crystal lattice produced by the variant k can be seen as a parametric strain

$$\underset{\sim}{\boldsymbol{\varepsilon}}^{tp} := \begin{pmatrix} \varepsilon & \gamma & 0 \\ \gamma & 0 & 0 \\ 0 & 0 & 0 \end{pmatrix} \tag{95}$$

Various theories are available to determine vectors $\underline{\boldsymbol{n}}$ and $\underline{\boldsymbol{t}}$, depending on the material crystallography (for instance Wechsler-Lieberman-Read theory, 24 variants)

3 Finite element computations of single crystalline components

The purpose of this section is to illustrate the behaviour of single crystal laboratory specimens and of industrial components. After a quick look to the algorithmic expression of the model, one shows the case of cylindrical tension specimens, then tubular specimens. A few elements are given to figure the type of calculations that can be made on turbine blades.

3.1 Algorithm for the numerical integration

The integration of these equations in a finite element code can be made either by an explicit or an implicit method. If compared with classical inelastic equations, single crystal models must solve the additional problem of choosing the active slip systems. This is why, after classical viscoplastic solutions where all the slip systems are active (Pierce et al., 1985; Asaro and Needleman, 1985), many authors have proposed their original solutions (Méric and Cailletaud, 1991; Cuitino and Ortiz, 1992; Anand and Kothari, 1996; Schröder and Miehe, 1997; Simo and Hughes, 1997; McGinty and McDowell, 2006). The interest of the implicit approach is that it provides the jacobian matrix needed for computing the consistent tangent matrix. Classically, the system of ordinary differential equations is solved by a Newton technique, which is applied to the incremental form coming from the application of a θ–method. For the sake of simplicity, the present model is restricted to small strain, and linear isotropic hardening. In such a case, the integration variables are the increment of elastic strain $\Delta\varepsilon^e$ and the increments of (visco)plastic shear strain, Δp^s, which are positive for all the slip systems. For the case of time independent plasticity, these two variables will be deduced from two types of equations:

- The strain partition:

$$\Delta\underset{\sim}{\varepsilon} = \Delta\underset{\sim}{\varepsilon}^e + \sum_r \underset{\sim}{m}^r \Delta p^r \tag{96}$$

- The expression of the criteria for the active slip systems:

$$f^s = |\tau^s| - r^s = 0 \tag{97}$$

$$\text{with } \tau^s = \underset{\sim}{m}^s : \underset{\approx}{\Lambda} : \underset{\sim}{\varepsilon}^e \qquad r^s = \sum_r h_{sr} p^r labeleq : hardx \tag{98}$$

As a result, the system to solve is formed of equations (99) and (100):

$$\mathcal{F}_e = -\Delta\underset{\sim}{\varepsilon} + \Delta\underset{\sim}{\varepsilon}^e + \sum_r \underset{\sim}{m}^r \Delta p^r \tag{99}$$

$$\mathcal{F}_p^s = \left| \underset{\sim}{m}^s : \underset{\approx}{\Lambda} : (\underset{\sim}{\varepsilon}^e + \Delta\underset{\sim}{\varepsilon}^e) \right| - \tau_0 - \sum_r h_{sr}(p^r + \Delta p^r) \tag{100}$$

If the model is viscoplastic instead of being plastic, equations (100) must be replaced by (101), the equation coming from the strain partition being unchanged:

$$\mathcal{F}_p^s = \left| \underset{\sim}{m}^s : \underset{\approx}{\Lambda} : (\underset{\sim}{\varepsilon}^e + \Delta\underset{\sim}{\varepsilon}^e) \right| - \tau_0 - \sum_r h_{sr}(p^r + \Delta p^r) - K \left(\frac{\Delta p^s}{\Delta t} \right)^{1/n} \tag{101}$$

This algorithm is implemented in the `Zmat` library of the `ZéBuLoN` code (Foerch et al., 1997) which has been used for all the simulations of this chapter.

3.2 Laboratory specimens

It is well known that the stress and strain state is not homogeneous in "tensile" specimens which are not oriented along high symmetry directions like {001} or {111}. If the rotations are blocked, the strain heterogeneity can even be very high, as illustrated in Fig.9a (Méric and Cailletaud, 1991). Other cases are still more remarkable: torsions of a thin wall tube. According to the orientation of the tube axis, the number of "soft" zones around the circumference will change. This can be easily understood by computing the resolved shear stress along the circumference. For the case of a {001} oriented specimen, there is four soft zones (Fig.9b), and for a {111} oriented specimen, six soft zones (Fig.9c). Note that a series of criteria proposed in the literature for single crystal modelling, which are based on Hill's quadratic criterion do not capture this effect, since all the points of the circumference have the same shear stress. Experiments have been made to confirm the prediction given by the model. This is illustrated by Fig.10, which shows the location of the jauges (Fig.10a), meanwhile Fig.10b and c respectively show the loops measured by the jauges, respectively in the $< 110 >$ and in the $< 100 >$ areas: the strain measured by the jauge is on the horizontal axis, and the torsion couple is on the vertical axis. The Schmid factor is rather small in the second case, thus the behaviour is not far from purely elastic. On the contrary, $< 110 >$ is a soft zone, with a large hysteresis loop. The reader is invited to go back to (Nouailhas and Cailletaud, 1995) for a more detailed view on the tests available. Yield surfaces have been determined in tension–torsion. It is worth noting that, according to the ratio between tensile and shear loadings, the softer zones can be either $< 110 >$ or $< 100 >$!

Other specimens have also be considered in the past, for instance bicrystalline specimens (Méric et al., 1994).

3.3 Turbine blades

Single crystals are used in industry, specially in the hotest sections of the turbines (for planes or power plants), where they accept higher temperatures than classical alloys (Cailletaud et al., 2001; Busso et al., 2003). Figure 11 shows a typical computation result performed in cooperation with Snecma (Safran group): after stress–strain computations, specific post-processing are used to estimate the creep–fatigue life of the component. The most re-

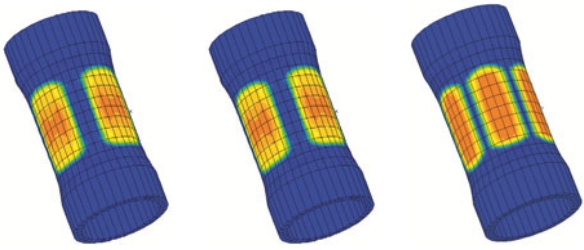

(a) (b) (c)

Figure 9. Various loading cases producing strain heterogeneties on laboratory specimens: (a) {123} oriented specimen loaded in tension; (b) {001} oriented specimen loaded in torsion; {111} oriented specimen loaded in torsion;

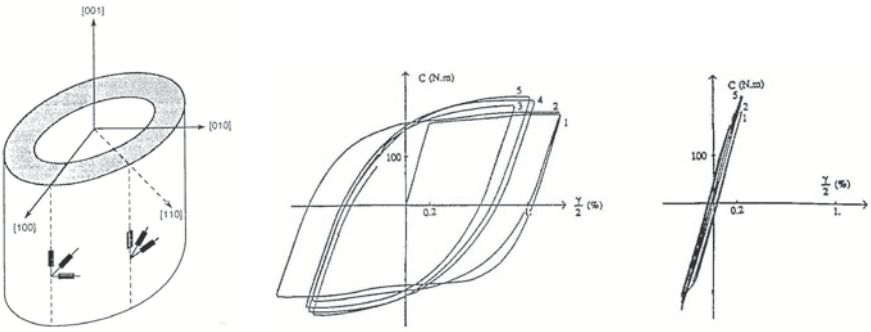

(a) (b) (c)

Figure 10. (a) Location of the jauges on the tube; (b) soft response of the jauge located in $< 110 >$ area; (c) allmost elastic response of the jauge located in $< 100 >$ area

Figure 11. (a) Life prediction on a turbine blade submitted to a thermo-mechanical loading

cent advances in blade design are related to more and more complex shapes, in relation with aerodynamics which make 3D computations mandatory, and also with more and more clever cooling systems. Modern blades are hollow, with a complex network of holes to have cool gas coming from inside the blade and form a protective film against the combustion gases. This is the reason why the critical zones are no longer predictable by inspired guessing from the shape of the blade.

On the other hand, this complex geometry introduces sometime so many details that they cannot be meshed with a reasonable precision. This is illustrated in Fig.12a, where a series of 1 mm diameter holes are present on the leading edge of the blade. The computation with the full geometry can be made for a reference computation, but the relevant mesh to capture all the details (several millions of nodes) cannot be used for parametric studies. In such a case, the weak zone can be globally modelled by means of homogenised models taking into account the holes. Drilling a hole in a single crystal will produce a material that does not possess the cubic symmetry. The axis of the hole is a preferential axis: along this axis, the material behaviour is unchanged, except that a correction of effective surface has to be made. For a tension or a compression along the two perpendicular axes, the behaviour becomes pressure sensitive. The resulting model must then be an orthotropic pressure sensitive single crystal. An homogenized model can be calibrated by means of cell calculations, like in Fig.12b and Fig.12c. The cells are loaded with periodic boundary conditions.

Assuming that the axis of the hole is $\underline{\boldsymbol{e}}_2$, a pressure effect is created for

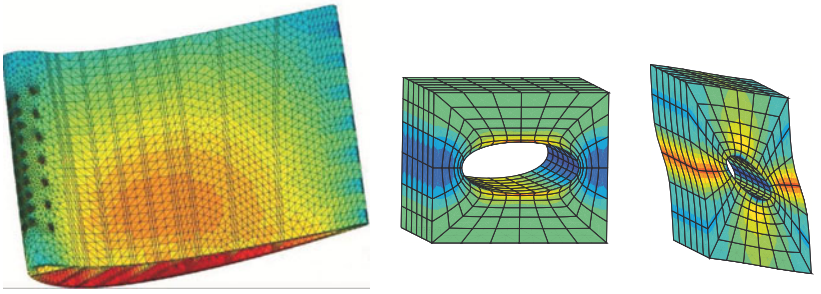

(a) (b) (c)

Figure 12. Development of a model to account for hole distribution (Cardona, 2000): (a) industrial component; (b) cell with a hole in tension; (c) cell with a hole in shear

the other two directions, $\underline{\boldsymbol{e}}_1$ and $\underline{\boldsymbol{e}}_3$ by introducing two new mechanisms in addition to the normal slip: this is an opening/closure of the hole, driven by the normal stress in the relevant direction, namely:

- two normal stresses are computed, $\sigma_1 = \underline{\boldsymbol{e}}_1.\underset{\sim}{\boldsymbol{\sigma}}.\underline{\boldsymbol{e}}_1$ and $\sigma_3 = \underline{\boldsymbol{e}}_3.\underset{\sim}{\boldsymbol{\sigma}}.\underline{\boldsymbol{e}}_3$
- two variables δ^1 and δ^3 are associated to these normal stresses:

$$\dot{\delta}^i = \left\langle \frac{\sigma_i - r^i}{K} \right\rangle^n$$

- δ^1 and δ^3 have their own contribution to the strain rate tensor, evaluated by means of $\underset{\sim}{\boldsymbol{n}}^1 = \underline{e}_1 \otimes \underline{e}_1$ and $\underset{\sim}{\boldsymbol{n}}^3 = \underline{e}_3 \otimes \underline{e}_3$ through the terms:

$$\dot{\delta}^1 \underset{\sim}{\boldsymbol{n}}^1 + \dot{\delta}^3 \underset{\sim}{\boldsymbol{n}}^3$$

The holes in the blades generate stress concentrations which lead to crack initiation. It is then useful to study cracks in single crystals. Due to the specificity of the yield criterion, the plastic zones ahead of the crack tip have a particular aspect. This was predicted by early studies made by Rice (Rice, 1987). Experimental veerifications and the related numerical simulations have been recently made(Flouriot et al., 2003). Figure 13, taken from this last paper, shows for instance that there is no plasticity in the direction of the crack ahead of the crack tip in an angle of about $\pm 30°$, for the case of a $\{001\}$ oriented specimen of FCC material.

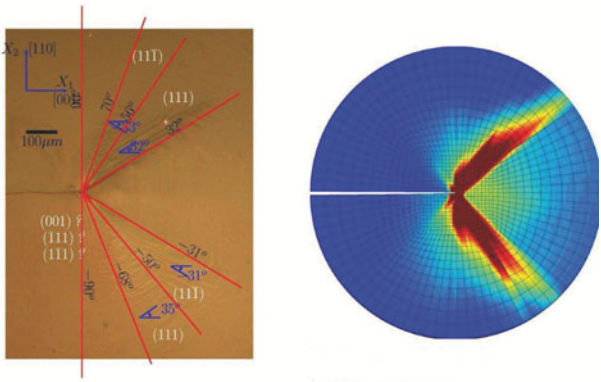

(a) (b)

Figure 13. View of the plastic activity ahead of a crack tip. (a) Experimental result; (b) Numerical simulation

4 Finite Element Crystal Plasticity

In the litterature, internal stresses in materials are classified into level I, II and III. Level III is the *microscopic level*, where intragranular stress present fluctuations inside each grain, with different values in the core of the grain and near grain boundaries, for instance. Level II denotes the result obtained at the grain level, after averaging the intragranular stresses. This can be made grain by grain; In this case, the resulting tensor is defined in each in individual grain, and takes into account the real neighborhood. Most of the time, measurements are rather able to capture stress on a given set of grains having the same crystallographic nature. This leads to an alternative definintion for level II, that is now obtained after an additional averaging operation. Level I refers to macroscopical stress, the stress tensor resulting from the averaging on a representative material element, large enough to include all the significant phases and grains.

Numerical models are attached to each of these scales. Macroscopic models naturally relates to level I. Uniform field models represent level II. The finite element method with embedded crystal plasticity models (Finite Element Crystal Plasticity, FECP) can be used to capture stress and strain fields on level III. It has been applied to calibrate the other levels too. This is illustrated in the present section.

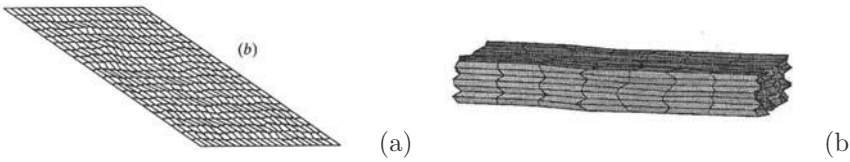

Figure 14. Use of regular meshes for studying large deformations of polycrystals and the related texture evolution: (a) 2D (Kalidindi et al., 1992), (b) 3D (Miehe et al., 1999)

Polycrystal, simplified microstructures In the past, finite element models have been used either to evaluate the homogenized behaviour of an aggregate with a predefined microstructure, or to make comparisons with local measurements in specimens with large grains.

Attempts to derive the global behaviour of an aggregate from the properties of its elementary constituents by means of 3D finite element computations can be found in the seventies (Engel, 1978). The material was represented by tetrahedric grains assembled in a cube, with a new crystal orientation for each finite element. The severe limitation at that time was the power of the computer, so that researchers had to wait for new generation of machines. Figure 14 shows further typical studies, made on 2D meshes ((Kalidindi et al., 1992)) or 3D meshes ((Miehe et al., 1999)). In these cases, authors wanted to check the global behaviour of the aggregates, and predict the texture evolution in large deformation. The aggregate has nothing to do with a realistic microstructure, since each finite element has its own crystallographic orientation (*one element–one grain*), figuring a set of cubic grains with regularly distributed neighbours. The model is rather seen as an evolution of Taylor's model, where the kinematic conditions (uniform plastic strain) is known to be too restrictive. In fact, the results obtained with such crude meshes are not far from Taylor solution: this is not surprinsing, since there is not enough degrees of freedom to reproduce the high heterogeneity present in real aggregates. On the other hand, the prediction of the texture evolution is often satisfactory. It remains that the main reliable information that can be taken from these computations are the so called first order stress and strain fields, that is the homogenized fields.

Some more complex meshes have then been used, to represent more precisely the local behaviour. A series of computations are illustrated in Fig.15. Figure 15a shows the finite element model used to compute the av-

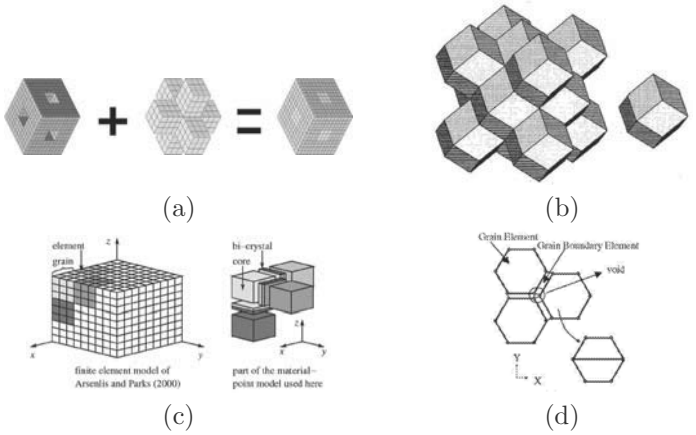

Figure 15. Examples of meshes used in the literature to represent various microstructures: (a) two phase material (Bugat et al., 1999), (b) attempt to capture a realistic grain microstructure (Mika and Dawson, 1999), (c) grain boundaries on a 3D cubic mesh (Evers et al., 2002), (d) grain boundaries on 2D hexagonal grains (Kim et al., 2002)

erage stress tensors in a two phase material (Bugat et al., 1999). The first phase (left) is represented by 20 elementary cubes, the second by 7 elementary cubes. Introducing symmetries, each phase forms a coninuous periodic network. The respective volume fraction can be controlled by the size of the internal cubes. The purpose of the computation is to evaluate a stress level in each phase, to be used as an input in brittle failure models, that is level II stress. The next example in figure (15b) is between level II and III, since a more realistic shape is introduced (Mika and Dawson, 1999). The last two examples (Fig.15c and d) try to separate the interior of the grain and a grain boundary area. Again, more realistic meshes would provide more reliable computation of the rspective influence of each zone (Evers et al., 2002; Kim et al., 2002).

Multicrystal, real microstructures The other traditional type of study consists in computing real specimens with a relatively low number of grains. Contrary to the previous case, there is a large number of elements in each grain, so that the intragranular gradients can be obtained. This allows authors to illustrate multislip effect (Delaire et al., 2000) inside the grain or

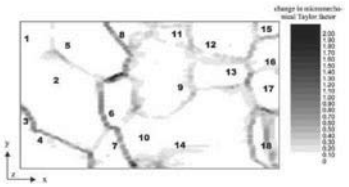

Figure 16. Examples of experiments and simulation using multicrystalline specimens: (a) experimental results on a copper specimen (Delaire et al., 2000), (b) illustration of the perturbation due to grain boundaries on Taylor factor (Raabe et al., 1981)

at the grain boundaries (Raabe et al., 1981). The state of the art for such a class of calculations if as follows:

- there is a good agreement between experiments and numerical simulations, specially for large grains;
- grain boundaries are still not well characterised; secondary slip might be present in rather large zones;
- the behavior of a grain in its environment differs from the behaviour of the corresponding single crystal;
- the unknown grains under the surface do affect the behaviour of the surface grains.

Polycrystal, realistic microstructures An other trend in FECP is the modeling of polycrystalline aggregates, involving a large number of grains (several hundreds) to capture the polycrystal effect, using realistic synthetic microstructures to capture the effects of the local morphology and of the neighborhood, and involving a reasonnable number of elements in order not to introduce artefacts due to the poor discretization. The interested reader will consult papers like (Barbe et al., 2001a,b; Diard et al., 2002; Cailletaud et al., 2004). The most popular solution to generate the numerical model starts from a Voronoï tesselation. As shown in Fig.17a and b, this construction provides domains around points that are initially dropped in the material element. The distribution can be random. Alternatively, a repulsion distance can be introduced, anisotropic distributions can be considered... Other types of distributions are also in development: they consider ellipsoids growing at various rates, or other types of assumptions based on models for grain growth. Having a microstructure in hand, the next step of a microstructure computation is to generate the finite element

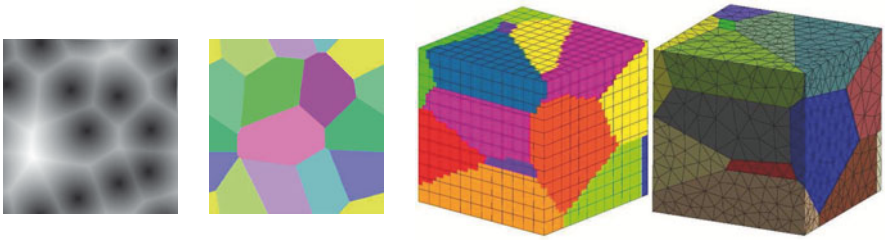

(a) (b) (c) (d)

Figure 17. Mesh generation using Voronoï tesselation: (a) Distance function of a set of point sources, (b) Tesselation result after construction and labelling, (c) multiphase element technique, (d) 3D mesh respecting grain boundaries

mesh. In the past, authors have used either multiphase element technique (Fig.17c) or free mesh generation (Fig.17d). According to the first solution, material properties are affected to the Gauss points according to their position in a cube which defines the material element. This is a quite flexible approach, nevertheless, grain boundaries are cumbersome, so that it is not applicable for a good characterization of the grain boundaries. On the other hand, free mesh generation do respect grain boundaries, and is a good starting point to look for real intragranular fields (level III).

Figure 18 presents a typical result on a regular 28×28×28 mesh. Multiphase element technique has been used. The general behaviour or the strain fields is to form strain localization lines, as shown in Fig.18b. This has nothing to do with instabilities, since the material presents hardening everywhere, on a local and a global scale. This is just the fact that deformation propagates from one grain to the other, sometime without consideration of the local orientation. On the other hand, stress levels do respect grain boundaries. The von Mises equivalent stress field shown in Fig.18c is clearly sensitive to the crystallographic morphology.

Convergence studies have been performed in (Barbe et al., 2001a,b). The most remarkable points are the following:

- For moderate strains (a few percent), quadratic meshes with full integration provide more precise results than linear meshes, for the same number of nodes. Nevertheless, an oscillation due to the spherical part of the stress tensor may appear when classical element are used. Mixed elements introducing the trace (and eventually the volume change) as a degree of freedom provide more stable results. Alternatively, a post-

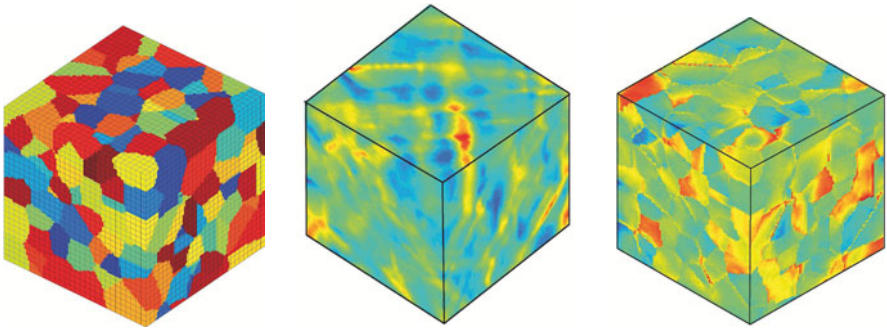

(a) (b) (c)

Figure 18. Typical results on a polycrystalline aggregate: (a) a 28×28×28 mesh with 200 grains, (b) local field of total axial strain, (c) local field of von Mises stress

treatment of the result can be made, to replace the trace on each Gauss point by the trace of the element.

- Reaching a stable curve for level I stress (macroscopic level) is rather easy. This can even be achieved with a one element–one grain mesh ! The variations observed on a tensile curve reaches only a few percent with two hundred grains for various mesh size.
- Level III stresses and strains are much more difficult to capture. For coarse meshes, the localization areas are not well defined, they are too large, but the maximum values are too small: the finer the mesh, the higher the maximum stress (or strain), the lower the minimum stress (or strain). This is illustrated in Fig.19, on a slice made in several 3D meshes, with an increasing number of elements.
- Fully constraint boundary conditions (imposed strain) provide the most homogeneous fields, and the highest resulting stress (at level I). Figure 20 shows the resulting axial strain–axial stress curves for each of the 200 grains of a polycrystalline aggregate (level II). In Fig.20a, the stress–strain state of the grains follows the Berveiller–Zaoui approach, which will be explained later (section 5.2): for a given time step, they are along a line whose slope decreases with strain. According to this uniform field model, each grain is surrounded by all the other grains. This is not the case in the finite element method, so that the distribution is not so smooth. Tension under strain control (Fig.20b) produces m ore scatter in stress (low scatter on strain),

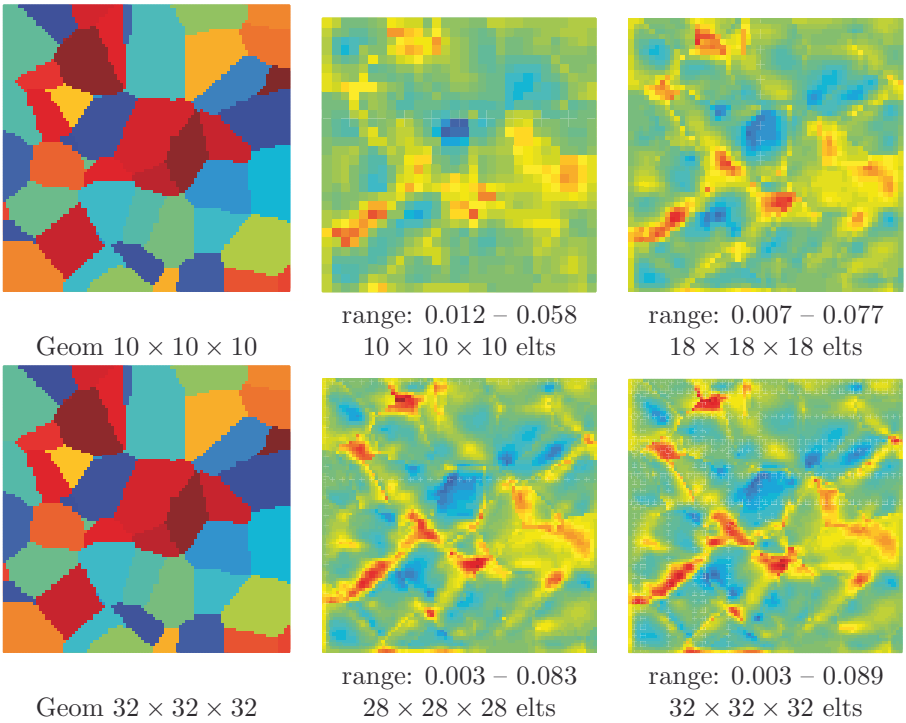

Figure 19. Evolution of the local strain field (von Mises equivalent) for various mesh sizes, for an axial tension (0.2% in the vertical direction, 200 grains) on a quadratic mesh

meanwhile tension under stress control (Fig.20c) produces more scatter in strain. The graphs in Fig.20d, e, f show the results for the lateral stresses, whose average is equal to zero. This plot shows that the stress state is triaxial inside the aggregate, even for a tensile strain.

- As far as level III is concerned, free faces promote scatter: for a given mesh, the computation performed with a free face will produce lower values *and* smaller values than the computation made under prescribed strain. The same observation is made inside the grains. Grain boundaries promote also scatter: in its vicinity, maximum stress or strain increase, minimum stress or strain decrease (see Fig.21).

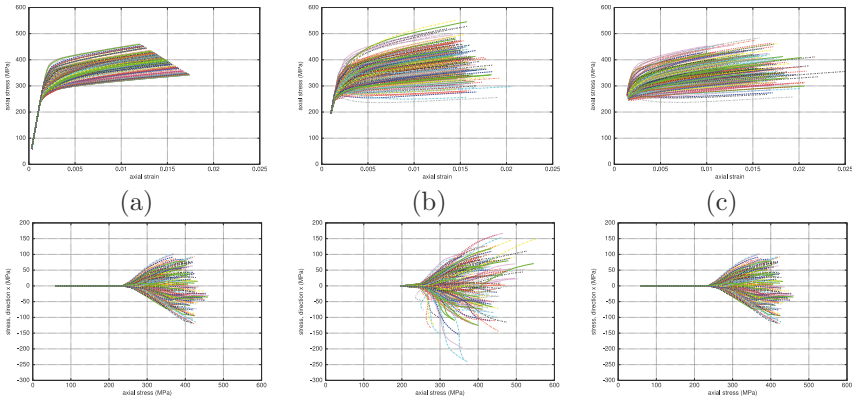

Figure 20. Local stress-strain curves for 200 grains for different boundary conditions, compared to the self-consistent approach: axial components (a) for the self-consistent model, (b) for homogeneous boundary conditions (c) for 4 free faces; lateral components (d) for the self-consistent model, (e) for homogeneous boundary conditions (f) for 4 free faces

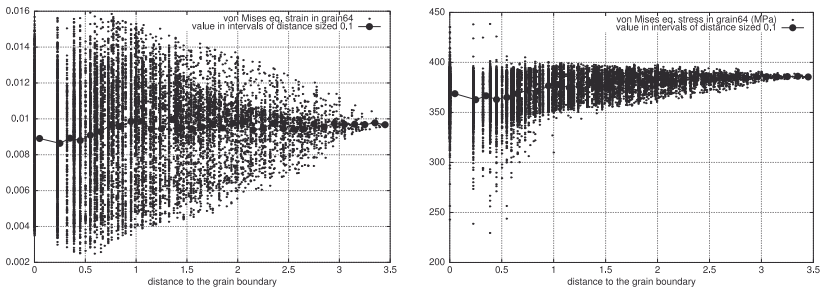

Figure 21. (a) Equivalent plastic strain (von Mises) *versus* dist to the GB; (b) Equivalent stress (von Mises) *versus* dist to the GB

Recent developments

In the preceding examples, Finite Element Crystal Plasticity has been used either directly to compute specimens or components made of a single crystal, or in representative material elements. For this last case, the output can be the macroscopic stress and strain fields, the stress and strain fields in the grains or the local intragranular fields (level I, II, III respectively). Results at level I and II are devoted to a calibration of macroscopic or uniform field models. Level III is more and more interesting, since the meshes are now large enough to capture details near critical zones like grain boundaries. On the other hand, this is the relevant scale to open dialogs with other scales and other types of plasticity models, like the dynamic dislocation simulations. Level II or III can be the relevant scale to introduce failure prediction models, like cleavage or integranular damage. Some example of recent trends are now mentioned in this section.

Figure 22 shows the modeling of a test on a OFHC copper specimen. Serial cuts were done to get the microstructure geometry below the surface, so that the grain shape is known on a parallelipipedic box whose depth is 100 μm, and the surface 200 μm$\times$150 μm. Crystal orientations were characterized by OIM. The material is modelled by the constitutive equations shown in section (2.2). The material parameters are fitted on the macroscopic tension curve. Simulated results (strain and rotation fields) are in good agreement with the measurements made by image comparison technique (Musienko et al., 2007).

As stated previously, grain boundaries are the place where specific phenomena may arise. This is the case when SCC mechanisms are active, for instance in fuel assemblies of PWR. The expansion of the uranium dioxide pellets may produce an interaction with Zy4 (a zirconium alloy) cladding, producing the so called *Pellet–Cladding Interaction*, that generates intergranular cracks, whose propagation is promoted by iodine due to the nuclear reaction, then cleavage and failure of the tube. The mechanical effect is related to an indentation of the tube by pellets: as a consequence, the affected zone is very small, and important gradients can be observed on the first few grains under the surface. An appropriate model has then to take into account the crystallographic character. The numerical model developed (Cailletaud et al., 2004) introduces a coupled FE calculation: iodine adsorption at the grain boundaries is represented by a diffusion calculation (where the diffusivity strongly depend on damage of the grain boundary, so that the high concentration profile follows the crack propagation) and a mechanical calculation (where *grain boundary affected zones* are represented by specific constitutive equations). A catastrophic process is produced by

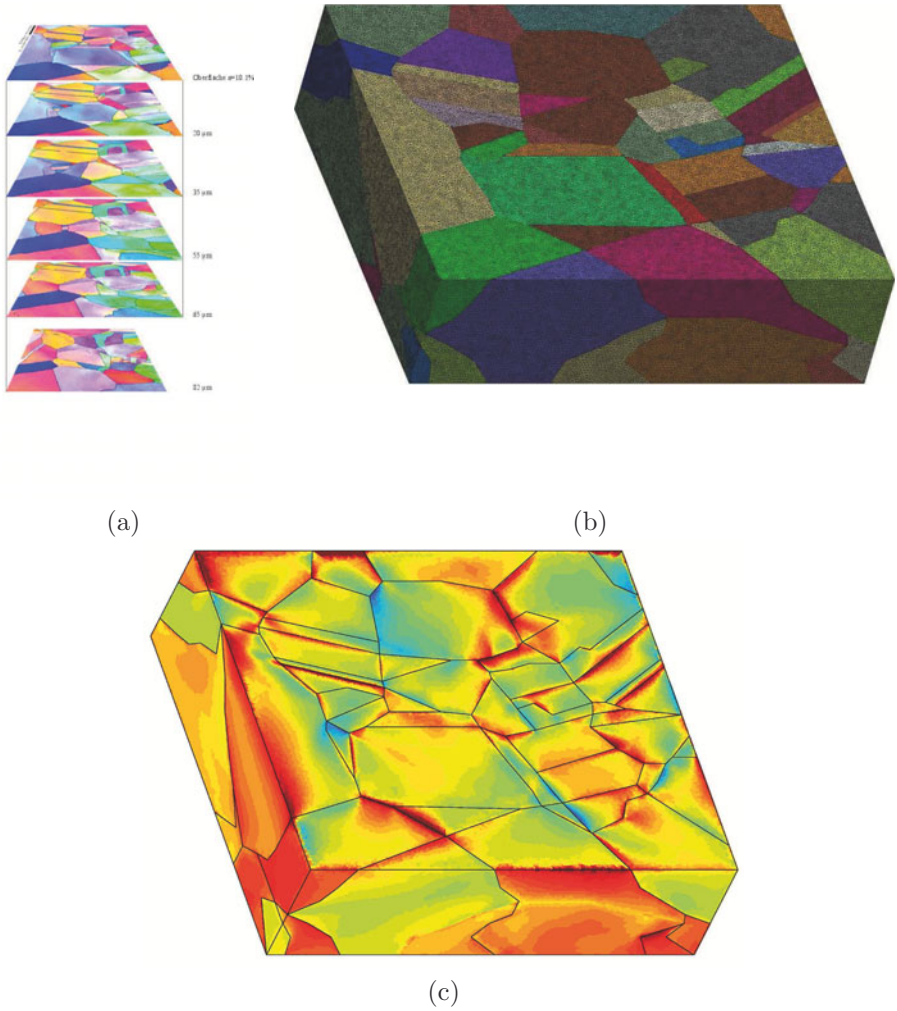

Figure 22. FE computation of a copper specimen. (a) OIM analysis on serial cuts in the specimen, (b) associated mesh, (c) contour of equivalent plastic strain for a macroscopic strain of 5% (range for local strain is 0–0.214)

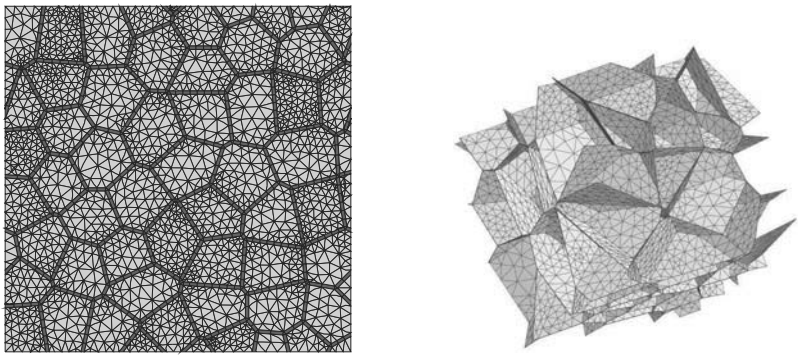

(a) (b)

Figure 23. Example of mesh generation with grain boundaries : (a) 2D, (b) 3D

the fact that iodine concentration promotes damage, and damage promotes iodine advance in the grain boundaries. 2D and 3D meshes are available (Fig.23).

The model introduces an affected zone in *each* grain, so that the *grain boundary* is made of two elements. In these area, the model collects first the slip systems of the grain it belongs to: basal, (predominant) prismatic and pyramidal slip planes are present, since the material has a HCP microstructure. Three other scalar variables are present, to represent Damage, Opening and Sliding of the grain boundary (DOS model). Grain boundary opening mechanisms is built with the tensorial product of the normal vector $\underline{\boldsymbol{n}}$ to the grain boundary by itself, meanwhile grain boundary sliding is built with the tensorial product of $\underline{\boldsymbol{n}}$ by the tangent vector in the grain boundary plane, $\underline{\boldsymbol{t}}$. Damage is introduced in the model to increase the rate of opening and sliding. Its evolution depends on a critical variable which account for the normal and the shear stresses on the grain boundary. The resulting equations are given below:

- Elasticity and plastic flow

$$\text{Strain decomposition:} \qquad \dot{\underset{\sim}{\varepsilon}} = \dot{\underset{\sim}{\varepsilon}}^e + \dot{\underset{\sim}{\varepsilon}}^p \tag{102}$$

$$\text{Elastic law with isotropic damage:} \qquad \underset{\sim}{\boldsymbol{\sigma}} = (1-D)\underset{\approx}{\boldsymbol{L}} : \underset{\sim}{\boldsymbol{\varepsilon}}^e \tag{103}$$

$$\text{Opening and sliding:} \qquad \dot{\underset{\sim}{\varepsilon}}^p = \dot{\delta}\underline{\boldsymbol{n}} \otimes \underline{\boldsymbol{n}} + \dot{\gamma}^{\{}\underline{\boldsymbol{n}} \otimes \underline{\boldsymbol{t}}^{\}} \tag{104}$$

- Flow rules for opening and sliding

$$\text{Opening:} \qquad \dot{\delta} = \left\langle \frac{< \sigma_{11} > /(1-D) - R_n}{K_n} \right\rangle^{n_n} \tag{105}$$

$$\text{Sliding:} \qquad \dot{\gamma} = \left\langle \frac{|\tau|/(1-D) - R_t}{K_t} \right\rangle^{n_t} sign(\tau) \tag{106}$$

- Damage evolution

$$\text{Critical variable:} \qquad \sigma_D = \sqrt{\sigma^2 + \beta\tau^2} \tag{107}$$

$$\text{Damage evolution:} \qquad \dot{D} = \left\langle \frac{\sigma_D - R_D}{A} \right\rangle^{r} (1-D)^{-k} \tag{108}$$

Figure 24 illustrates typical results obtained with the 2D aggregate of Fig.23. Maps (a-c) illustrate the intergranular crack propagation which is obtained by solving the mechanical problem only. In this case, cracks initiate everywhere in the material element, and the propagation is a mixture of crack growth and coalescence. For maps (d-f), iodine is introduced at the left edge of the mesh, so that the grain boundaries are more critical at this point. One main crack propagates. It is worth noting that crack branching can be seen for each triple point. The crack propagation rate is in good agreement with the experimental results. 3D simulations are still necessary, in order to capture the real aspect of the cracks in space and avoid the artefacts related to 2D computations (a crack is too critical, since it crosses the whole mesh in the third direction !).

Fatigue–fretting is an other case where the description of the material by a crystal plasticity model can be very helpful. Figure 25 shows the numerical model developed to simulate a disk–plan test, both of them being made of a titanium alloy. Grain size is around 50 μm, so that the stress gradient under the surface corresponds to a few grains in depth (Dick and Cailletaud, 2006).

A typical effect related to the use of crystal plasticity instead of a traditional J_2 model is shown in Fig.26: after some fretting cycles, local heterogeneities propagate much more in crystal plasticity than with a von Mises material; eventually, local ratchetting can be observed, so that, starting from the analytical value of the stress profile computed in elasticity (Hertz solution), von Mises model leads to a smoothly modified curve, but crystal plasticity produces a highly heterogeneous field, in which the maximum stress can locally increase. This may have important consequence for the response of subsequent damage models, trying to predict either wear of crack initiation.

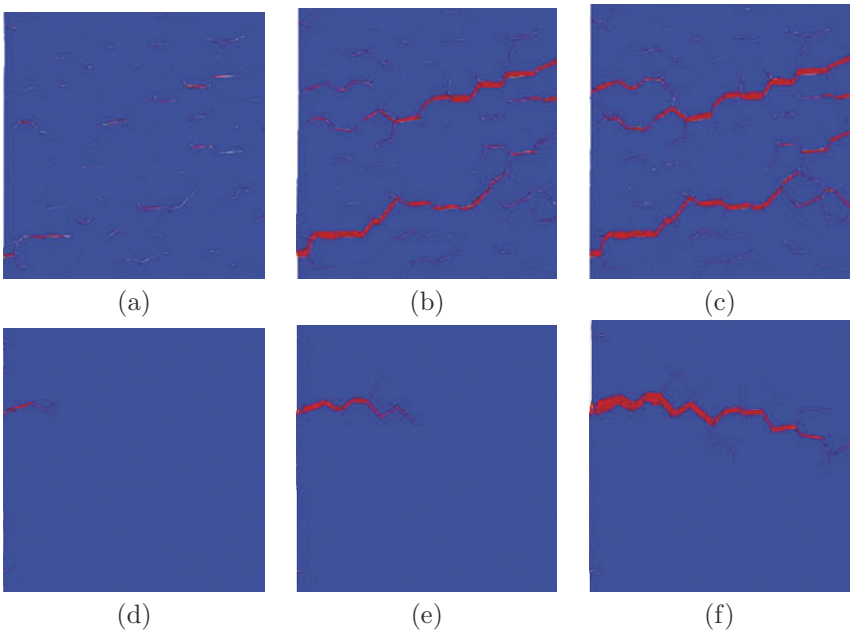

Figure 24. Crack propagation predicted by intergranular damage evolution : (a,b,c) non-coupled case; (d,e,f) coupled case

5 Uniform field models

Developing models at level II can be considered as an interesting alternative, that allows the user to represent the constitutive equations of each phase, and avoids unjustified mixture rules. The resulting models are more complex than the models on the macroscale, but they are still manageable, either in drivers of constitutive equations or even in finite element codes.

5.1 Yield surfaces

This section illustrates the transition from a single crystal surface, as shown in Fig.6, that results from a collection of hyperplanes in the stress space, to surfaces for directionnally solidified (DS) or polycrystalline materials. An uniform elasticity is assumed for each grain, so that the local stresses are equal to the macroscopic stress in the elastic regime. In DS material, grains are supposed to have the same (001) axis, and random ori-

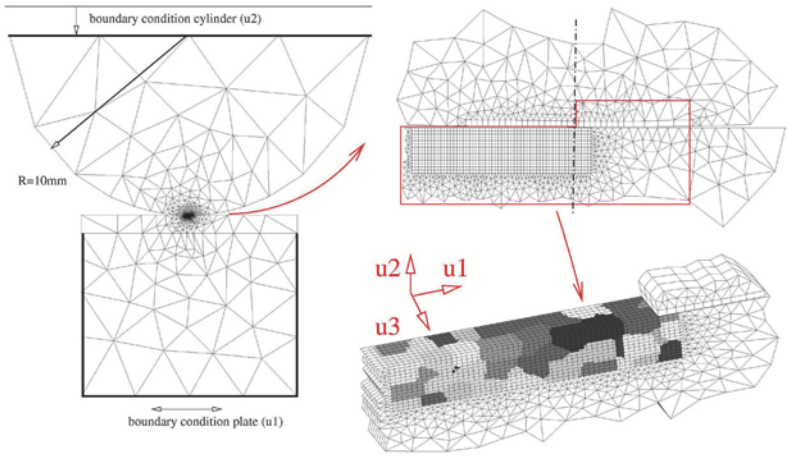

Figure 25. Geometry of the mesh used for the numerical simulation and grain morphology

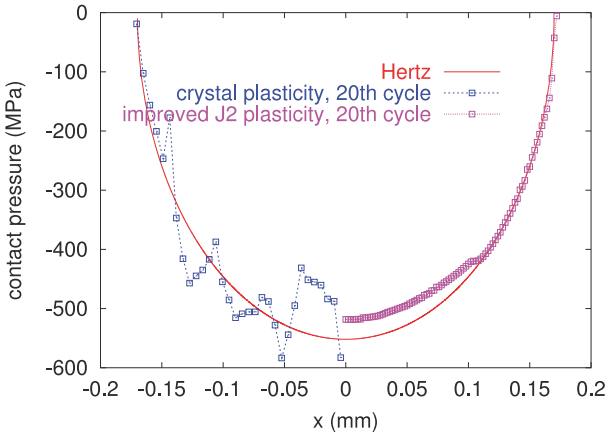

Figure 26. Comparison if the evolution of the contact pressure for J2 plasticity and for a crystallographic model

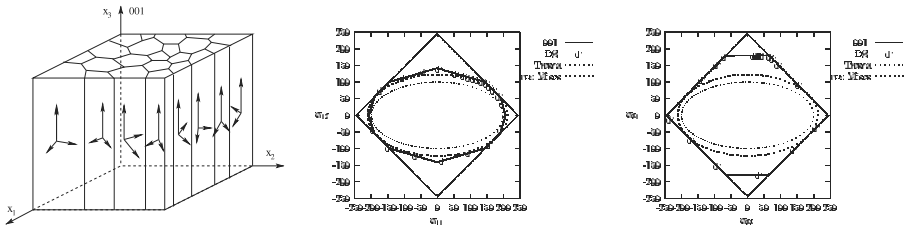

(a) (b) (c)

Figure 27. Yield surface for a DS material: (a) geometry of the aggregate, (b) yield surface in the σ_{11}–σ_{12} plane, (c) yield surface in the σ_{33}–σ_{31} plane

entation in the plane perpendicular to (001). The loading axes (x_1,x_2,x_3) coincide with the crystallographic axes. The resulting model for such an aggregate still presents crystal characteristics in the plane σ_{33}–σ_{31} (Fig.27c), due to the reduced number of slip systems available for shear. On the other hand, the shape of the criterion in σ_{11}–σ_{12} plane (Fig.27b) looks like a macroscopic isotropic model. The present figure was plotted with only three orientations, whose axis (100) makes an angle of 0°, 30°, 60° with x_1. The references to Tresca and von Mises are built by supposing that the critical shear stress for Schmid's law in each single crystal is taken as the critical shear for Tresca (the difference between the two extreme eignestresses), and as the octahedral shear for von Mises (the square root of the half of the sum of the squares of the three differences between the eigenstresses). A full characterization of the elasto-plastic behaviour of this material can be found elsewhere (Sai et al., 2006).

On the other hand, if the construction is made for a polycrystal with random orientations (Fig.28), the resulting criterion is isotropic, and reaches exactly Tresca criterion (the present plot uses 1000 grains).

5.2 Scale transition rules

As observed previously in FE computations, plastic or viscoplastic flows are heterogeneous in the aggregates. The plots of Fig.20 demonstrate that neither stresses nor strains are uniform from one grain to the other. The rôle of the scale transition rule is to provide an estimation of the stress tensor in each grain. The purpose of this section is to make a quick overview of the various rules and of their physical meaning. The following notations will be used:

- Stress in phase g, macroscopic stress: $\underset{\sim}{\boldsymbol{\sigma}}^g$, $\underset{\sim}{\boldsymbol{\sigma}} = \sum_g f^g \underset{\sim}{\boldsymbol{\sigma}}^g$

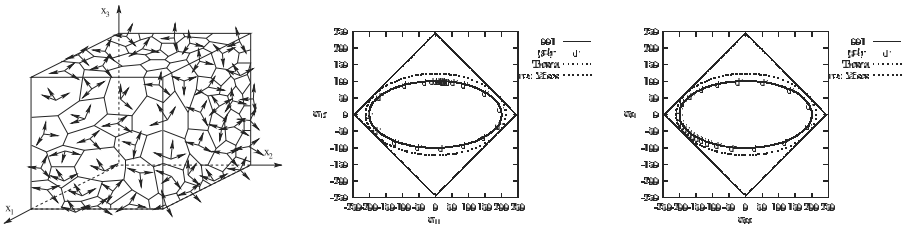

(a) (b) (c)

Figure 28. Yield surface for an isotropic polycrystalline material: (a) geometry of the aggregate, (b) yield surface in the σ_{11}–σ_{12} plane, (c) yield surface in the σ_{33}–σ_{31} plane

- Strain in phase g, macroscopic strain: $\underset{\sim}{\varepsilon}^g$, $\underset{\sim}{E} = \sum_g f^g \underset{\sim}{\varepsilon}^g$
- For an uniform local elasticity, the macroscopic plastic strain is also the average of the local plastic strains: $\underset{\sim}{\varepsilon}^p = \sum_g f^g \underset{\sim}{\varepsilon}^{pg}$

More detailed comments are given elsewhere Besson et al. (2001). The most popular models correspond to the following assumptions:

- Static, *uniform stress*, $\underset{\sim}{\sigma}^g = \underset{\sim}{\Sigma}$
- From Taylor to Kröner
  - Taylor (Taylor, 1938), *uniform plastic strain*, $\underset{\sim}{\varepsilon}^{pg} = \underset{\sim}{E}^p$
  - Lin–Taylor (Lin, 1957), *uniform total strain*, $\underset{\sim}{\varepsilon}^g = \underset{\sim}{E}$
  - Kröner (Kröner, 1971), *elastic accommodation*

$$\underset{\sim}{\sigma}^g = \underset{\sim}{\Sigma} + \underset{\approx}{\Lambda} : (\underset{\approx}{I} - \underset{\approx}{S})(\underset{\sim}{\varepsilon}^p - \underset{\sim}{\varepsilon}^{pg})$$

    where $\underset{\approx}{\Lambda}$ is the elastic tensor and $\underset{\approx}{S}$ the Eshelby tensor (Mura, 1987).
  - Kröner for an isotropic material (elastic and plastic) and pressure insensitive plasticity

$$\underset{\sim}{\sigma}^g = \underset{\sim}{\Sigma} + \mu\alpha(\underset{\sim}{\varepsilon}^p - \underset{\sim}{\varepsilon}^{pg}) \quad \text{with} \quad \alpha = \frac{2(7-5\nu)}{15(1-\nu)}$$

- Tangent and secant approximations (self-consistent framework)
  - Hill (Hill, 1965), *elastoplastic accommodation*

$$\dot{\underset{\sim}{\sigma}}^g = \dot{\underset{\sim}{\Sigma}} + \underset{\approx}{L}^\star : (\dot{\underset{\sim}{E}} - \dot{\underset{\sim}{\varepsilon}}^g)$$

    where $\underset{\approx}{L}^\star$ is a tangent accommodation tensor.

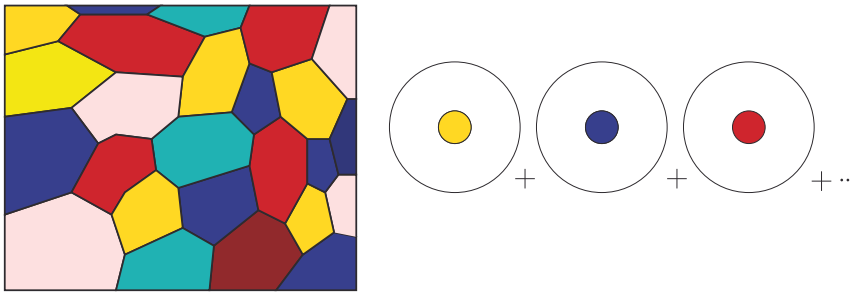

(a) (b)

Figure 29. An illustration of polycrystal modelling: (a) actual aggregate, (b) collection of auxiliary problems

– Berveiller–Zaoui (Berveiller and Zaoui, 1979) estimation, with α varying typically between 1 and 0.001 (valid for the particular case of isotropic elasticity, pressure insensitive plasticity and spherical inclusions), as shown later in equation (113)

$$\underset{\sim}{\boldsymbol{\sigma}}^g = \underset{\sim}{\boldsymbol{\sigma}} + \mu\alpha(\underset{\sim}{\boldsymbol{\varepsilon}}^p - \underset{\sim}{\boldsymbol{\varepsilon}}^{pg}) \quad \text{with} \quad \alpha =$$

- Viscous and viscoplastic scheme
  - Budianski, Hutchinson, Molinari... (Hutchinson, 1966; Molinari et al., 1987)
  - Translated fields (Sabar et al., 2002),

$$\dot{\underset{\sim}{\boldsymbol{\sigma}}}^g = \dot{\underset{\sim}{\boldsymbol{\sigma}}} + 2\mu(1-\beta)(\frac{5\eta}{3\eta + 2\eta^g}\dot{\underset{\sim}{\boldsymbol{\varepsilon}}}^v - \dot{\underset{\sim}{\boldsymbol{\varepsilon}}}^{vg})$$

- Parametric scale transition rule
  - Cailletaud, Pilvin, *β–model* , that will be developed below.

The way the models are obtained in the self-consistent framework is illustrated in Fig.29, which shows that all the realizations of a given grain orientation in the aggregate are put together into a single sphere, that is embedded in the homogeneous medium. The solution of the problem is then obtained as a collection of auxiliary problems, leading to an implicit scheme, since the behaviour of the homogeneous medium is not known. The calculation result will have the shape:

$$\dot{\underset{\sim}{\boldsymbol{\sigma}}} = \dot{\underset{\sim}{\boldsymbol{\Sigma}}} + \underset{\approx}{\boldsymbol{L}}^\star : (\dot{\underset{\sim}{\boldsymbol{E}}} - \dot{\underset{\sim}{\boldsymbol{\varepsilon}}}) \tag{109}$$

with $\underset{\sim}{\underset{\sim}{\boldsymbol{L}}}^{\star}$, accommodation tensor:

$$\underset{\sim}{\underset{\sim}{\boldsymbol{L}}}^{\star} = \underset{\sim}{\underset{\sim}{\boldsymbol{L}}}^{eff} : (\underset{\sim}{\underset{\sim}{\boldsymbol{S}}}^{-1} - \underset{\sim}{\underset{\sim}{\boldsymbol{I}}}) \tag{110}$$

The value of $\underset{\sim}{\underset{\sim}{\boldsymbol{L}}}^{eff}$ is obtained by solving the following implicit equation (Hill, 1965):

$$\underset{\sim}{\underset{\sim}{\boldsymbol{L}}}^{eff} = < \underset{\sim}{\underset{\sim}{\boldsymbol{L}}} : (\underset{\sim}{\underset{\sim}{\boldsymbol{L}}} + \underset{\sim}{\underset{\sim}{\boldsymbol{L}}}^{\star})^{-1} : (\underset{\sim}{\underset{\sim}{\boldsymbol{L}}}^{eff} + \underset{\sim}{\underset{\sim}{\boldsymbol{L}}}^{\star}) > \tag{111}$$

For the classical case of uniform elasticity, incompressible plastic flow, radial loading path, a simplified expression can be written, with μ', actual shear modulus, and $\beta' = 2(4-5\nu')/15(1-\nu')$

$$\dot{\underset{\sim}{\boldsymbol{\sigma}}}^{g} = \dot{\underset{\sim}{\boldsymbol{\sigma}}} + 2\mu \frac{\mu'(1-\beta')}{\beta'\mu + (1-\beta')\mu'} (\dot{\underset{\sim}{\boldsymbol{\varepsilon}}}^{p} - \dot{\underset{\sim}{\boldsymbol{\varepsilon}}}^{pg}) \tag{112}$$

For pure tension, assuming $\nu = 1/2$ and introducing the *secant* modulus $H = \sigma/\varepsilon^p$, the model can be simplified:

$$\dot{\sigma}_g = \dot{\sigma} + \frac{\mu H}{H + 2\mu} (\dot{\varepsilon}^p - \dot{\varepsilon}^{pg}) \tag{113}$$

At the onset of plastic flow, H tends to infinity, so that Kröner's rule is recovered. The accommodation factor $C = (\sigma^g - \sigma)/(\varepsilon^p - \varepsilon^{pg})$ decreases when plastic strain increases. This expression is easy to manage, nevertheless its domain of application is limited. This is why the β–rule has been proposed (Cailletaud, 1987; Pilvin and Cailletaud, 1990; Cailletaud and Pilvin, 1994).

The goal of this model is to represent the plastic accommodation, like Hill's approach, but in an explicit formulation. Instead of having a non linear multiplicative term and a linear dependency from the difference between local and global plastic strain, like in Berveiller–Zaoui's approach, it was decided to keep the linear multiplicative term (like in Kröner's formulation), and to introduce a new phenomenological variable instead of plastic strain to account for non linear accommodation.

The local stress decreases when the grain becomes more plastic than the matrix, so that a typical shape of the model is:

$$\underset{\sim}{\boldsymbol{\sigma}}^{g} = \underset{\sim}{\boldsymbol{\sigma}} + C \left(\underset{\sim}{\boldsymbol{\beta}} - \underset{\sim}{\boldsymbol{\beta}}^{g} \right) \tag{114}$$

with

$$\underset{\sim}{\boldsymbol{\beta}} = \sum_{g} f_g \underset{\sim}{\boldsymbol{\beta}}^{g} \tag{115}$$

f_g is the volume fraction of phase g, $\underset{\sim}{\boldsymbol{\beta}}^g$ characterizes the state of redistribution.

The new interphase accommodation variables $\boldsymbol{\beta}^g$ follow a kinematic evolution rule. Two evolution laws have been tested in the past.

$$\text{- rule 1: } \dot{\underset{\sim}{\boldsymbol{\beta}}}^g = \dot{\underset{\approx}{\boldsymbol{\varepsilon}}}^g - D\dot{\varepsilon}^g_{eq}\underset{\sim}{\boldsymbol{\beta}}^g \tag{116}$$

$$\text{- rule 2: } \dot{\underset{\sim}{\boldsymbol{\beta}}}^g = \dot{\underset{\approx}{\boldsymbol{\varepsilon}}}^g - D\dot{\varepsilon}^g_{eq}(\underset{\sim}{\boldsymbol{\beta}}^g - \delta\underset{\approx}{\boldsymbol{\varepsilon}}^g) \tag{117}$$

In the two rules, the equivalent strain rate in the fading memory term can be replaced by the sum of the slip rates on all the slip systems. Rule 2 is nothing but a combination of a linear an a non linear term; a quick manipulation shows that the expression can be recovered by assuming $\underset{\sim}{\boldsymbol{\beta}} = \delta\underset{\sim}{\boldsymbol{\beta}}^1 + (1-\delta)\underset{\sim}{\boldsymbol{\beta}}^2$ and:

$$\dot{\underset{\sim}{\boldsymbol{\beta}}}^1 = \dot{\underset{\approx}{\boldsymbol{\varepsilon}}}^p \quad \text{and} \quad \dot{\underset{\sim}{\boldsymbol{\beta}}}^2 = \dot{\underset{\approx}{\boldsymbol{\varepsilon}}}^p - D\underset{\sim}{\boldsymbol{\beta}}^2\ \dot{\varepsilon}^g_{eq}$$

The parameters C, D and δ are not free material coefficients, but *scale transition parameters*. Kröner's model can be found as a particular case by assuming that $D = \delta = 0$ and $C = \mu$. This is consistent with the fact that, at the onset of plasticity, the matrix behaviour deviates only a little from elastic behaviour, and an elastic accommodation is the proper response of the material. On the other hand, the rest of the parameters can be calibrated by means of more complex approaches, namely finite elements. For this purpose, a series of realistic aggregates (in terms of morphology and crystal orientations) must be selected. A large number of aggregates must be computed, to have a chance to place each grain orientation in an environment which is representative of all the grains (this is not the case for one unique computation, since, statistically, each real grain has between 15 and 25 neighbours only). A post-processing allows then to compute the macroscopic stress–strain curve, and the average values in each crystallographic phase. The identification of the coefficients can then be made by solving an inverse problem. The goal is to fit, not only the macroscopic curve, but also the local stresses and strains with the β-model. Note that this information is rather rich, so that it may be difficult to reproduce the local stresses (even if is it rather easy to get the global behaviour).

5.3 Complex paths

When coupled with a crystal plasticity model in each grain, the β-rule has been found able to provide interesting effects, which were observed in the litterature, but that cannot be modelled by macroscopic approaches, except by adding specific variables. Two classical examples are shown here: figure 30 illustrates the example of the so called *memory effect*, that is

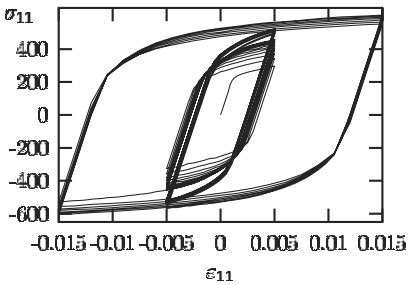

parameter	value
R_0	100
Q	50
b	10
c	5000
d	100
h_i	1,i

Figure 30. Illustration of the strain memory effect coming from the slip system activation

present for instance in austenitic stainless steels (Chaboche et al., 1979). Three successive loading levels are applied to a tension–compression specimen, the first amplitude is 0.5%, the second one is 1.5%, and the third one 0.5% again. The maximum stress at the third level is much bigger than the stress at the first one, even if the range is the same. The model reproduces correctly this effect due to a more intense slip system activation at the second level.

An extra slip system activation is also present for non proportional loading. This type of load (sinusoidal imposed tension and shear with a phase lag of 90°) is know to produce maximum stresses on each components much larger than the corresponding load type for a proportional loading. Figure 31 shows the response in the tension–shear stress plane, and the history of the von Mises stress as a function of time. The illustration of the slip system activity for the same test is shown in Fig.32, by comparison with the result of a tensile test. The material has a FCC microstructure, and the slip systems are represented on unfolded Thomson tetrahedra (four planes represented by triangles, with three subtriangles in each of them figuring the slip systems). The number of active slip system is 2.17 in average for a tension at 1.5%, meanwhile the number is 3.25 for the non proportional loading at the same equivalent strain. All these effects are discussed elsewhere Cailletaud (1992).

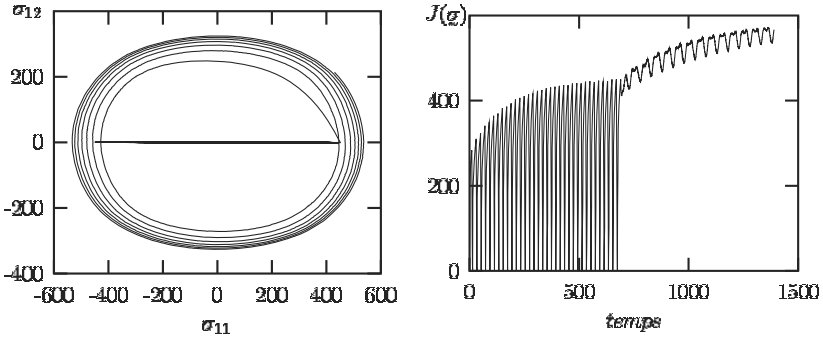

(a) (b)

Figure 31. Extra-hardening due to non-proportional loading: (a) response in the stress plane, (b) evolution of the equivalent stress

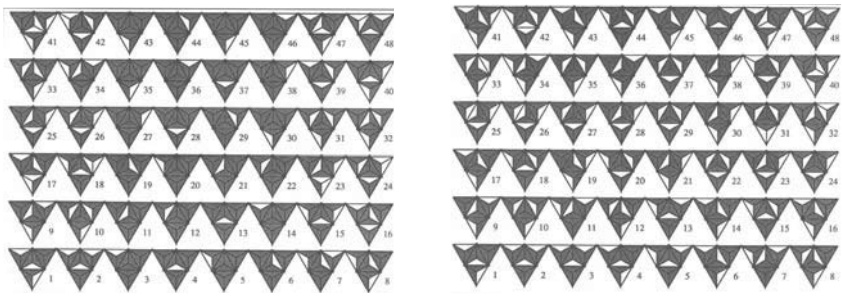

(a) Average number per grain: 2.17 (b) Average number per grain: 3.25

Figure 32. Illustration of the local behaviour of a FCC aggregate: active systems are in white (a) case of a proportional loading, (b) case of a non proportional loading

6 Conclusion and perspectives

Classical crystal plasticity is now a mature theory. The material parameters have been identified for many materials, so that the models can be used for a large number of academic or industrial applications. The goal of the present section was then to summarize a few possibilities of the models, with a special view toward the *operational* aspect, that is their practical use. A series of related subjects are not considered here, but would be of interest for continuing the discussion.

One of the main extension of the classical framework is proposed by the theory of generalized continua. There is an profuse litterature on the subject. The reader can check for instance a recent synthesis in (Papenfuss and Forest, 2006). These extended theories have already been applied to single crystal (see for instance Forest et al. (2000, 2002)). This new type of approach allows the user to take into account size effect, that is specially meaningfull for materials that present small grains or specific heterogeneous microstructures (like γ–γ').

The second type of connection is to be made with other classes of approaches. For collecting information at the scale of the grain, or, generally speaking, on submicronic sizes, the relevant theories do not refer to continuous, but to discrete modeling frameworks. This is the case of discrete dynamics of dislocations (DDD), and of molecular dynamics (MD), which have both their own space and time scales. In the future, the progress of these approaches will allow to provide inputs for the higher scales: one will *bridge the lenghtscales* by taking information for DDD from MD, and for crystal plasticity from DDD (see the rest of the present course).

Finally, a previously unattained chance of progress is now given to the theories devoted to material modeling by the advance of experimental tools and methods. Field measurements are now possible, with a very good definition (Musienko et al., 2007; Kempf et al., 2007). Using powerfull beams, experimentalists will be able to provide data like 3D-microstructure shape and crack population inside the material. Having in hand local data and local material modeling, one will be able to develop new classes of damage models, based on real mechanisms at the microstructure level.

Bibliography

L. Anand and M. Kothari. A computational procedure for rate–independent crystal plasticity. *J. Mech. Phys. Sol.*, 44:525–558, 1996.

R.J. Asaro. Micromechanics of crystals and polycrystals. *Advances in Appl. Mech.*, 23:1–115, 1983a.

R.J. Asaro. Crystal plasticity. *J. of Applied Mechanics*, 50:921–934, 1983b.

R.J. Asaro and A. Needleman. Texture development and strain hardening in rate dependent polycrystals. *Acta Metall.*, 33:923–953, 1985.

R.J. Asaro and J.R. Rice. Strain localization in ductile single crystals. *J. Mech. Phys. Sol.*, 25:309–338, 1977.

F. Barbe, L. Decker, D. Jeulin, and G. Cailletaud. Intergranular and intragranular behavior of polycrystalline aggregates. Part I: FE model. *Int. J. of Plasticity*, 17(4):513–536, 2001a.

F. Barbe, S. Forest, and G. Cailletaud. Intergranular and intragranular behavior of polycrystalline aggregates. Part II: Results. *Int. J. of Plasticity*, 17(4):537–566, 2001b.

M. Berveiller and A. Zaoui. An extension of the self–consistent scheme to plastically flowing polycrystal. *J. Mech. Phys. Sol.*, 26:325–344, 1979.

J. Besson, R. Le Riche, R. Foerch, and G. Cailletaud. Object–oriented programming applied to the finite element method. Part II: Application to material behaviors. *Revue Européenne des Éléments Finis*, 7(5):567–588, 1998.

J. Besson, G. Cailletaud, J.-L. Chaboche, and S. Forest. *Mécanique non–linéaire des matériaux*. Hermès, 2001.

J.F.W. Bishop and R. Hill. A theoretical derivation of the plastic properties of a polycrystalline face–centered metal. *Philosophical Magasine*, 42:414–427, 1951.

S. Bugat, J. Besson, and A. Pineau. Micromechanical modeling of the behavior of duplex stainless steels. *Computational Materials Science*, 16:158–166, 1999.

E. Busso, M. Toulios, and G. Cailletaud. Constitutive material formulations and advanced life assessment methods for single crystal gas turbine blades. In J. Lecomte-Beckers, M. Carton, F. Schubert, and Schriften des Forschung Zentrum Jülich Ennis, P.J., editors, *7th Conf. Materials for advanced power engineering, Liège, 30 sept.–2 oct. 2002*, pages 1175–1185, 2003.

E.P. Busso and F.A. McClintock. A dislocation mechanics-based crystallographic model of a B2-type intermetallic alloy. *Int. J. of Plasticity*, 12: 1–28, 1996.

G. Cailletaud. A micromechanical approach to inelastic behaviour of metals. *Int. J. of Plasticity*, 8:55–73, 1992.

G. Cailletaud. *Une approche micromécanique phénoménologique du comportement inélastique des métaux*. PhD thesis, Université Pierre et Marie Curie, Paris 6, 1987.

G. Cailletaud and P. Pilvin. Utilisation de modèles polycristallins pour le calcul par éléments finis. *Revue Européenne des Éléments Finis*, 3(4): 515–541, 1994.

G. Cailletaud, J.-L. Chaboche, S. Forest, and L. Rémy. On the design of single crystal turbine blades. *Revue de Métallurgie*, février 2003:165–172, 2001.

G. Cailletaud, O. Diard, and A. Musienko. Damage, opening and sliding of grain boundaries. In S. Ahzi, M.A. Khaleel, H.M. Zbib, M.A. Zikry, B. LaMatina, and M. Cherkaoui, editors, *Multiscale Modelling and Characterisation of Elastic-Inelastic Behaviour of Engineering Materials (Proc.of the IUTAM Symposium on Multiscale Modelling of Engng. Materials. Marrakech, Oct. 2002)*, pages 149–156. Kluwer, 2004.

J.-M. Cardona. *Comportement et durée de vie des pièces multiperforées : application aux aubes de turbine*. PhD thesis, École Nationale Supérieure des Mines de Paris, 2000.

J.-L. Chaboche, K. Dang Van, and G. Cordier. Modelisation of the strain memory effect on the cyclic hardening of 316 stainless steel. In *Proc. SMIRT 5*, volume L, page L11/3, Berlin, 1979.

G.Y. Chin and W.L. Mammel. Generalization and equivalence of the minimum work (Taylor) and maximum work (Bishop–Hill) principles for crystal plasticity. *Trans. of the Met. Soc. of AIME*, 245:1211–1214, 1969.

M. Clavel. *Fatigue plastique et fissuration de deux alliages durcis par des précipités cohérents. Etude comparative des mécanismes*. PhD thesis, ENSMA, 1980.

B.D. Coleman. Thermodynamics of materials with memory. *Arch. Rat. Mech. Anal.*, 17:1–46, 1964.

A.M. Cuitino and M. Ortiz. Computational modelling of single crystals. *Modelling Simul. Mater. Sci. Eng.*, 1:225–263, 1992.

F. Delaire, J.L. Raphanel, and C. Rey. Plastic heterogeneities of a copper multicrystal deformed in uniaxial tension: experimental study and finite element simulations. *Acta Metall.*, 48:1075–1087, 2000.

B. Devincre, L. Kubin, and T. Hoc. Physical analyses of crystal plasticity by dd simulations. *Scripta Metallurgica and Materiala*, 54:741–746, 2006.

O. Diard, S. Leclercq, G. Rousselier, and G. Cailletaud. Distribution of normal stress at grain boundaries in multicrystals: application to an intergranular damage modeling. *Computational Materials Science*, 25: 73–84, 2002.

T. Dick and G. Cailletaud. Fretting modelling with a crystal plasticity model of Ti6Al4V. *Computational Materials Science*, 38:113–125, 2006.

J.-J. Engel. *Modélisation du comportement global des métaux en plasticité et en viscoplasticité*. PhD thesis, École Nationale Supérieure des Mines de Paris, 1978.

L.P. Evers, D.M. Parks, W.A.M. Brekelmans, and M.G.D Geers. Crystal plasticity model with enhanced hardening by geometrically necessary dislocation accumulation. *J. Mech. Phys. Sol.*, 50:2403–2424, 2002.

S. Flouriot, S. Forest, G. Cailletaud, A. Köster, L. Rémy, B. Burgardt, V. Gros, and J. Mosset, S. Delautre. Strain localization at the crack tip in single crstal ct specimens under monotonous loading: 3d finite element analyses and application to Nickel-base superalloys. *Int. J. Frac*, 124: 43–77, 2003.

R. Foerch, J. Besson, G. Cailletaud, and P. Pilvin. Polymorphic constitutive equations in finite element codes. *Comp. Meth. Appl. Mech. Engng*, 141: 355–372, 1997.

S. Forest, F. Barbe, and G. Cailletaud. Cosserat modelling of size effects in the mechanical behaviour of polycrystals and multiphase materials. *Int. J. Sol. Structures*, 37:7105–7126, 2000.

S. Forest, R. Sievert, and E.C. Aifantis. Strain gradient crystal plasticity: thermomechanical formulations and applications. *J. of the Mechanical Behaviour of Materials*, 13:219–232, 2002.

P. Franciosi. The concepts of latent hardening and strain hardening in metallic single crystals. *Acta Metall.*, 33:1601–1612, 1985a.

P. Franciosi. On flow and work hardening expression correlations in metallic single crystal plasticity. *Revue de Physique Appliquée*, 33:1601–1612, 1985b.

P. Germain, Q.S. Nguyen, and P. Suquet. Continuum thermodynamics. *J. of Applied Mechanics*, 50:1010–1020, 1983.

B. Halphen and Q.S. Nguyen. Sur les matériaux standards généralisés. *Journal de Mécanique*, 14:39–63, 1975.

F. Hanriot. *Étude du comportement du superalliage AM1 sous sollicitations cycliques*. PhD thesis, École Nationale Supérieure des Mines de Paris, 1993.

F. Hanriot, G. Cailletaud, and L. Rémy. Mechanical behavior of a nickel-base superallot single crystal. In A.D. Freed and K.P. Walker, editors, *High Temperature Constitutive Modeling – Theory and Application*. ASME, 1991.

K.S. Havner. *Finite Plastic Deformation of Crystalline Solids*. Cambridge University Press, 1992.

R. Hill. A self–consistent mechanics of composite materials. *J. Mech. Phys. Sol.*, 13:213–222, 1965.

R. Hill. Generalized constitutive relations for incremental deformation of metal crystals by multislip. *J. Mech. Phys. Sol.*, 14:95–102, 1966.

R. Hill and J.R. Rice. Constitutive analysis of elastic–plastic crystals at arbitrary strains. *J. Mech. Phys. Sol.*, 20:401–413, 1972.

J.W. Hutchinson. Bounds ans self-consistent estimates for creep of polycrystalline materials. *Proc. Royal Soc. London*, A348:101–127, 1966.

E.H. Jordan and K.P. Walker. Biaxial constitutive modelling and testing of a single crystal superalloy at elevated temperature. In K. Miller, editor, *Conf. on Multiaxial Fatigue, Sheffield*, 1985.

S.R. Kalidindi, C.A. Bronkhorst, and L. Anand. Crystallographic texture evolution in bulk deformation processing of FCC metals. *J. Mech. Phys. Sol.*, 40:536–569, 1992.

D. Kempf, V. Vignal, G. Cailletaud, R. Oltra, J.C. Weeber, and E. Finot. High spatial resolution strain measurements at the surface of duplex stainless steels. *Philosophical Magasine*, 87:1379–1399, 2007.

D.J. Kim, T.W. Ku, and B.S. Kang. Finite element analysis of micro-rolling using grain and grain boundary elements. *J. of Materials Processing Technology*, 130–131:456–461, 2002.

U.F. Kocks. The relation between polycrystal deformation and single-crystal deformation. *Metallurgical Transaction*, 1:1121–1143, 1970.

U.F. Kocks and T.J. Brown. Latent hardening in aluminium. *Acta Metall.*, 14:87–98, 1966.

W.T. Koiter. *General theorems for elastic–plastic solids*, volume 6, pages 167–221. North–Holland Publishing Company, 1960.

E. Kröner, editor. *Statistical continuum mechanics*, volume 92 of *CISM Courses and lectures*. Springer Verlag, 1971.

T. Kubo, Y. Wakashima, K. Amano, , and M. Nagai. Effects of crystallographic orientation on plastic deformation and initiation of zirconium alloys. *J. Nucl. Mat.*, 132(1):1–9, 1985.

J. Lemaitre and J.-L. Chaboche. *Mechanics of Solid Materials*. Cambridge University Press, Cambridge, U.K., 1990.

T.H. Lin. Analysis of elastic and plastic strain in FCC crystal. *J. Mech. Phys. Sol.*, 5:143, 1957.

J. Mandel. Une généralisation de la théorie de la plasticité de W.T. Koiter. *Int. J. Sol. Structures*, 1:273–295, 1965.

J. Mandel. *Plasticité classique et viscoplasticité*, volume 97. Cours du CISM, 1971.

R.D. McGinty and D.L. McDowell. A semi-implicit integration scheme for rate independent finite crystal plasticity. *Int. J. of Plasticity*, 22:996–1025, 2006.

L. Méric and G. Cailletaud. Single crystal modeling for structural calculations. Part 2: Finite element implementation. *J. of Engng. Mat. Technol.*, 113:171–182, 1991.

L. Méric, P. Poubanne, and G. Cailletaud. Single crystal modeling for structural calculations. Part 1: Model presentation. *J. of Engng. Mat. Technol.*, 113:162–170, 1991.

L. Méric, G. Cailletaud, and M. Gaspérini. FE calculations of copper bicrystal specimens submitted to tension–compression tests. *Acta Metall.*, 42 (3):921–935, 1994.

C. Miehe, J. Schröder, and J. Schotte. Computational homogenization analysis in finite plasticity simulation of texture development in polycrystalline materials. *Comp. Meth. Appl. Mech. Engng*, 171:387–418, 1999.

D.P. Mika and P.R Dawson. Polycrystal plasticity modeling of intracrystalline boundary textures. *Acta Metall.*, 47:1355–1369, 1999.

A. Molinari, G.R. Canova, and S. Ahzi. A self–consistent approach to the large deformation polycrystal viscoplasticity. *Acta Metall.*, 35:2983–2994, 1987.

T. Mura. *Micromechanics of defects in solids.* Martinus Nijhoff, 1987.

A. Musienko, A. Tatschl, K. Schmidegg, O. Kolednik, R. Pippan, and G. Cailletaud. 3D finite element simulation of a polycrystalline copper specimen. *Acta Mat.*, 55:4121–4136, 2007.

D. Nouailhas and G. Cailletaud. Tension-torsion behavior of single-crystal superalloys: experiment and finite element analysis. *Int. J. of Plasticity*, 11(4):451–470, 1995.

C. Papenfuss and S. Forest. Thermodynamical frameworks for higher grade material theories with internal variables or additional degrees of freedom. *J. of Non-Equilibrium Thermodynamics*, 31:319–353, 2006.

D. Pierce, R.J. Asaro, and A. Needleman. Material rate dependence and localized deformation in crystalline solids. *Acta Metall.*, 31:1951, 1985.

P. Pilvin and G. Cailletaud. Intergranular and transgranular hardening in viscoplasticity. In M. Zyczkowski, editor, *Creep in Structures*, volume 4, pages 171–178, 1990.

D. Raabe, M. Sachtleber, Z. Zhao, F. Roters, and S. Zaefferer. Micromechanical and macromechanical effects in grain scale polycrystal plasticity experimentation and simulation. *Acta Metall.*, 49:3433–3441, 1981.

J. Rice. Tensile crack tip fields in elastic-ideally plastic crystals. *Mech. of Materials*, 6:317–335, 1987.

J.R. Rice. On the structure of stress-strain relations for time–dependent plastic deformation in metals. *J. of Applied Mechanics*, 37:728, 1970.

J.R. Rice. Inelastic constitutive relations for solids: An internal variable theory and its application to metal plasticity. *J. Mech. Phys. Sol.*, 19: 433–455, 1971.

H. Sabar, M. Berveiller, V. Favier, and S. Berbenni. A new class of micro–macro models for elastic–viscoplastic heterogeneous materials. *Int. J. Sol. Structures*, 39:3257–3276, 2002.

K. Sai, G. Cailletaud, and S. Forest. Micro-mechanical modeling of the inelastic behavior of directionally solidified materials. *Mech. of Materials*, 38:203–217, 2006.

J. Schröder and C. Miehe. Aspects of computational rate-independent crystal plasticity. *Computational Materials Science*, 9:168–176, 1997.

J.C. Simo and T.R.J. Hughes. *Computational Inelasticity*. Springer Verlag, 1997.

L. Tabourot, M. Fivel, and E. Rauch. Generalised constitutive laws for FCC single crystals. *Material Science and Engineering*, A234-236:639–642, 1997.

G.I. Taylor. Plastic strain in metals. *J. Inst. Metals.*, 62:307–324, 1938.

C. Teodosiu, editor. *Constitutive Modeling of Polycrystalline Metals at Large Strains*, volume 376 of *CISM Courses and lectures*. Springer Verlag, 1997.